Microfluidics and Nanofluidics (2021) 25:61
https://doi.org/10.1007/s10404-021-02461-8

RESEARCH PAPER

# Some insights into the use of pore network simulations for predicting single-phase fluid flow in model porous media

**Hadi Adloo[1] · Behnam Abbasi[2]**

Received: 6 December 2020 / Accepted: 11 June 2021 / Published online: 23 June 2021


## Abstract

This study revisited the single-phase fluid flow in two-dimensional model porous media using pore network simulation (PNS). Some throats were randomly blocked to increase the tortuosity. Then single-phase fluid flow simulations were carried out in these networks using direct numerical simulation (DNS). Different correlations are usually used to estimate the pressure drop in throats, contractions, and expansions. We critically reconsidered the correlations available in the literature and introduced new correlations based on the results obtained from DNS. Trapezoidal and circular half-pore sections were studied separately, and it was concluded that the correlations are very sensitive to the pore body's geometry. The correlations extracted for throats and expansions precisely predict the permeability of corresponding elements in the network. The correlation for the contraction section did not match the respective DNS data in the network. A large discrepancy was observed by comparing the streamlines in the networks with the flow paths in isolated flow paths (not in the network). We found that the correlation for contraction section based on uniform flow at the inlet is not suitable for networks with complex pore structures. We showed that PNS's applicability with current correlations is limited to situations where throat resistance controls the permeability. By analyzing Darcy and Forchheimer's parameters, a large deviation was seen between PNS and DNS results. We demonstrated that eddies might form within the Darcy regime. In the model porous media studied in this paper, eddies and inertial core flow were known to play a prominent role in deviation from Darcy flow, which are not considered by PNS. It was concluded that short-range correlations are essential in modeling fluid flow at sub-pore level.

**Keywords** Direct numerical simulations · Porous media · Pore network simulations · Eddy formation · Inertial core flow · Non-Darcy flow

## List of symbols

| | |
|---|---|
| $A$ | Area of a pore [$m^2$] |
| $A_{\text{Network}}$ | Cross-area of a network perpendicular to main flow direction [$m^2$] |
| $C_c$ | Parameter used in in Eq. (11) |
| $d_C$ | Diameter of the largest circle surrounded by the pore walls [m] |
| $D_C$ | Dimensionless diameter aspect ratio for the largest circle surrounded by the pore walls [–] |
| $d_R$ | Width of a trapezoidal half pore [m] |
| $D_R$ | Dimensionless aspect ratio for width of trapezoidal half pore [–] |
| $d_t$ | Diameter of a throat [m] |
| $G_p$ | Shape factor [–] |
| $F_n$ | Normal force on the walls [N] |
| $F_t$ | Tangential force on the walls [N] |
| $K_D$ | Darcy permeability [$m^2$] |
| $K_F$ | Forchheimer permeability [$m^2$] |
| $l_t$ | Length of a throat [m] |
| $L_t$ | Dimensionless length aspect ratio for length of a throat [–] |
| $P$ | Pressure at the boundaries of each segment in PNS. Area-averaged pressure in DNS [Pa] |
| $p$ | Local pressure in DNS [Pa] |
| $Q$ | Mass flow rate [kg/s] |
| Re | Reynolds number [–] |
| $\boldsymbol{r_{PM}}$ | Vector that connects two points $P$ and $M$ |
| $U$ | Superficial velocity [m/s] |
| $u$ | Velocity component in main flow direction [m/s] |
| $v_t$ | Average velocity magnitude in a throat [m/s] |
| $\mathbf{V}$ | Velocity vector [m/s] |
| $\boldsymbol{v_P}$, $\boldsymbol{v_M}$ | Velocity vector at points $P$ and $M$ |

✉ Hadi Adloo
hadi.adlo@gmail.com

[1] Chemical Engineering Department, Islamic Azad University-Shiraz Branch, Shiraz, Iran

[2] Mechanic Department, Chamran University, Ahvaz, Iran

| | |
|---|---|
| **w** | Velocity component perpendicular to main flow direction [m/s] |
| $x_P$, $x_M$ | Two arbitrary points in the computation domain |

**Greek letters**

| | |
|---|---|
| β | Forchheimer parameter [$m^{-1}$] |
| $\Gamma_1$, $\Gamma_2$ | Parameters indicating the core and border of the eddies |
| φ | Viscous dissipation [Pa•$s^{-1}$] |
| η | Proportionality factor used in Eq. (6) |
| μ | Dynamic viscosity of fluid [Pa·s] |
| ρ | Density [kg/$m^3$] |
| σ | Parameter in Eq. (12) |
| Π | Perimeter of a pore body [m] |

**Superscripts**

| | |
|---|---|
| C | Contraction |
| E | Expansion |
| T | Throat |

## 1 Introduction

The well-known Darcy equation often simulates fluid transport at low velocity in porous media. However, at elevated superficial velocities, the linear assumption is inexact, and higher order approximations such as the Forchheimer equation must be used instead. Higher order terms are added to represent the additional resistance caused by the converging/diverging and tortuous flow at sub-pore level.

The origin and onset of non-Darcy flow are two topics of conversation among different researchers, and various methods are introduced to predict them. In brief, the source of the non-Darcy flow is mainly ascribed to the increase of inertial forces, which seems negligible at low Reynolds numbers (Hassanizadeh and Gray 1987; Lasseux and Valdés-Parada 2017; Ruth and Ma 1992; Skjetne and Auriault 1999). Numerical studies at pore-scale have also revealed that the formation of eddies can rise to non-Darcy regime, which increases the pressure drop (Fourar et al. 2004; Muljadi et al. 2016).

Porous media's intricate geometry can be characterized by high-resolution images acquired using various imaging methods such as micro-computed tomography (micro-CT). Direct numerical simulations (DNS)—as the most precise method—are often used for the prediction of fluid flow patterns in these image-based geometries (IBG) (Muljadi et al. 2016; Icardi et al. 2014; Scheibe et al. 2015; Aramideh et al. 2018). The main drawback of this method (DNS-IBG) is its high computational expense. Nevertheless, the flow patterns become highly correlated as different phenomena occur while passing the fluid through irregular channels. These issues oblige the researchers to use suitable representative elementary volumes (REV) and divide the void volume into sufficient numbers of cells to resolve fluid flow equations.

Pore network simulation (PNS) is a powerful computational tool to simulate transport phenomena in porous media. The void space of a porous medium is represented by pixels or voxels in IBG. In contrast, throats and pores are used in PNS to approximate the void space. Pores and throats are either generated stochastically or determined by algorithms such as medial axis and maximal ball (Dong and Blunt 2009; Bultreys et al. 2016; Raeini et al. 2017). Much simpler physical laws describe fluid transportation compared with multipurpose–multidimensional fluid flow equations, such as Navier–Stokes. To ensure the mass conservation over the entire computational domain, the mass entering and leaving any pore body must be equal (except for non-catalytic fluid–solid reaction with a stagnant product at the pore body). Thus, the main superiority of PNS to DNS-IBG is that it simplifies the multidimensional transport equations into several one-dimensional transport equations. However, estimating correct topology, morphology, and the correlations between void space are cited as PNS's main limitations (Raeini et al. 2017; Yi et al. 2017; Adloo et al. 2019; Adloo, 2015). The accuracy of the transport equations for pores and throats is another matter of discussion (Raeini et al. 2017; Blunt et al. 2002; Valvatne and Blunt 2004; Veyskarami et al. 2016, 2018).

PNS has been conducted to determine the transport parameters of porous media, including permeability and relative permeability (Lu et al. 2020). PNS is employed to describe the non-Darcy flow in porous media (Veyskarami et al. 2016; Thauvin and Mohanty 1998; Wang et al. 1999; Lao et al. 2004; Lemley et al. 2007a; Balhoff and Wheeler 2009; El-Zehairy et al. 2019). Most of the mentioned studies focused on the effect of contraction and expansion of flow at pore entrance. Some authors (Thauvin and Mohanty 1998; Wang et al. 1999; Lao et al. 2004) emphasized the importance of bending and branching of flow between adjacent throats in a pore. They asserted that it could account for up to 25% of the network's total pressure drop. However, as such correlations are limited to simple geometries like 90°-bend or 180°-bend, this method is mostly ignored. Different geometrical correlations were introduced to consider the contraction/expansion of pore entries and the effects of irregularities in pores/throats (such as crevices) (Raeini et al. 2017; Balhoff and Wheeler 2009; El-Zehairy et al. 2019).

Due to the non-Darcy flow complexity, we intend to know whether PNS is trustworthy enough to predict the fluid flow in porous media. Several image-based studies on flow patterns (Bultreys et al. 2016; Dybbs et al. 1984) and computational researches (Fourar et al. 2004; Muljadi et al. 2016; Yi et al. 2017; Chukwudozie and Tyagi 2013; Newman and Yin 2013) impressed the impact of flow patterns in the pore body in the occurrence of non-Darcy flow. It is found that

the contrast between throat and pore sizes in 2D geometries has a significant effect on flow regime transition and causing localized high-speed regions with intense energy dissipation (Newman and Yin 2013; Nissan and Berkowitz 2018; Cheng et al. 2019). All studies highlighted the role of eddies in pore bodies at high velocities. Eddies increase the residence time of the fluid resulting in more tortuous pathways. They are more likely to occur in the porous media that grains touch. In less compact geometries, streamlines appear to become localized in straight channels with high velocity at the center of the throats (known as inertial cores), and fewer eddies occur. Using numerical analysis, many researchers stated that high-speed flow in heterogeneous materials introduces eddies in the system, mainly in larger pores (Fourar et al. 2004; Muljadi et al. 2016; Newman and Yin 2013; Cheng et al. 2019). It is proved by numerical and experimental analysis that the surface roughness, even if decreasing the pore body volume, induces flow path variability, curvature, and eddy formation (Chukwudozie and Tyagi 2013; Liu et al. 2016). The contrast between the size of the pore body and throat amplifies the fluid inertia that results in localized energy dissipation near throat walls.

Furthermore, backflow at the throat entrance is seen due to flow separation. It is reported that the dissipated energy caused by narrower throats is much more significant than those of eddies (Newman and Yin 2013). Calculations by Fourar et al. (2004) showed that the pressure drop simulates the integral of dissipation function over all the fluid volume.

As cited above, different complicated phenomena may occur in heterogeneous materials as velocity increases. As far as we know, PNS cannot formally capture all these complexities. PNS is mainly based on mass conservation; the mass entering and leaving a junction (pore body) must be conserved. For permeability calculations in macropores, the driving force is the pressure gradient between adjacent intersections. Any other phenomenon that occurs must be entered into the model as fitting parameters. For example, Thauvin and Mohanty (1998) considered the pressure drop due to flow bending at each branch. They employed a correlation for turbulent pressure drop in 90° bends. Lao et al. (2004) and Lemley et al. (2007a) accounted for the pressure drop due to bends at each pore in networks of connectivity 3. They further incorporated the bending and flow splitting pressure drop in the momentum equation and proposed correlations for a few geometries (Lemley et al. 2007b). They related the pressure drop due to bends and splitting to the entropy generated in the pore (Lemley et al. 2007b).

There are still a couple of additional concerns. PNS accuracy significantly depends on the exactness of the algorithms used to extract the pore network (Baychev et al. 2019). In contrast to throats, modeling the flow in the pore body is usually sophisticated. The flow in the pore body is correlated to the local heterogeneity and topology. Some fitting factors are unavoidable to match the permeability obtained from PNS with those of experimental data.

This research aims to explore the applicability of different flow-pressure equations for throats and pores in PNS. We investigate PNS's limitations in predicting permeability using accurate flow-pressure equations for each transporting component (throats and half-pore bodies).

Section 2 devotes to the geometry definition and terminologies used in this study. Synthetic 2D porous media are employed because a pore network simulator could easily reproduce them. DNS and PNS are presented in Sect. 3. Section 4.1 suggests some relations to calculate the pressure gradient in each transport component. We compare their predictions with DNS results in Sect. 4.2. Section 4.3 presents the results for flow in networks of pores and throats using PNS and DNS. We conclude the paper in Sect. 5 with some suggestions for further studies.

## 2 Solid and void space geometry

In this work, we consider regular 2D pore networks with a size of $30 \times 30$. The geometry is composed of regular octagons, as depicted in Fig. 1a. The edges of the octagons are equal. The length of throats is defined by $l_t$ and their width is denoted by $d_t$. The width of a trapezoidal pore body is denoted by $d_R$. In PNS terminology, the expansions and contractions at the throat entrance are usually considered half of the pore bodies (see Fig. 1b). Together with a throat that connects two adjacent pore bodies, they form a flow path (FP). These terms are shown in Fig. 1b. Note that each pore may be characterized by a circle that is surrounded by the pore walls. The circle diameter is denoted by $d_C$. Figure 1c exhibits FPs in series as a periodic porous medium.

A schematic of a throat attached to neighbor pores is sketched in Fig. 1b. The throat walls consist of two parallel plates. In all structures, walls are smooth, and no off-axial connection is considered. $d_R$, $l_t$ and $d_t$ are dimensions that characterize the morphology of the media. In this work $l_t$ is constant ($l_t = 6$ mm). Some throats (23%) are randomly blocked to make the network more tortuous. Dimensional analysis leaves two non-dimensional morphological variables, say $L_t = l_t/d_t$ and $D_R = d_R/d_t$ or $D_C = d_C/d_t$. It is worth noting that $d_R$ and $d_C$ are functions of $d_t$ because the internal angles of the polygons are fixed (135°). Various morphologies are used to study the effect of different variables, as summarized in Table 1.

$d_C$ can be estimated as follows:

$$d_C = 4\frac{A}{\Pi}, \tag{1}$$

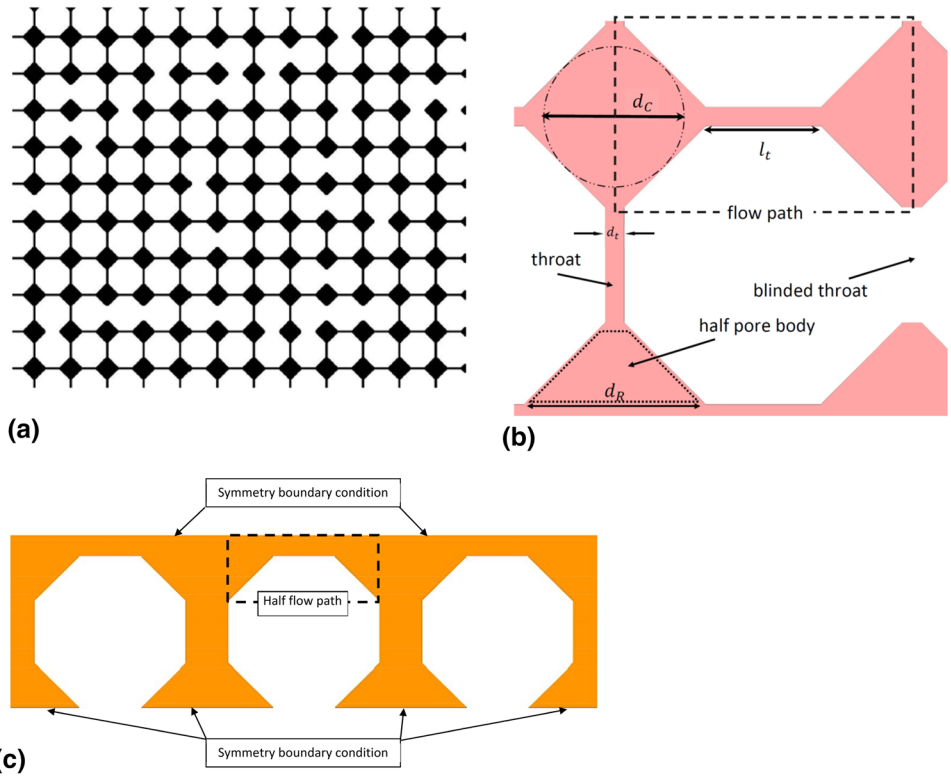


**Fig. 1** **a** 2D pore network (30×30) in which a faction of throats are randomly blocked; **b** terminology of the network and flow path (FP); **c** fluid paths in series ($D_R$=3.12 and $L_t$=1.5). In all sketches, the solid phase is shown in white, and the void phase is colored

**Table 1** Characteristic parameters for DNS and PNS studies. See Fig. 1b for more details

| Network | $L_t = l_t/d_t$ | $D_R = d_R/d_t$ | $D_C = d_C/d_t$ |
|---|---|---|---|
| 1 | 6/1 | 9.48 | 7.71 |
| 2 | 6/3 | 3.82 | 3.55 |
| 3 | 6/4 | 3.12 | 3 |

where $A$ is the pore area, and $\Pi$ is the pore perimeter. Real pores are not exactly circular, but the shape factor ($G$) can be employed to estimate their departure from circularity:

$$G_p = \frac{A}{\Pi^2}. \tag{2}$$

The shape factor for a circle is 0.0796. For other geometries, the shape factors are reported in Joekar-Niasar et al. (2010).

In this text, we often use the term isolated FP, which means a FP (a contraction section followed by a throat and an expansion section) that is not located in a network.

One of the advantages of such a simplified 2D model is that all morphological parameters are under control. Moreover, there is no uncertainty in the PNS results due to inexact mapping of morphology and topology into the pore network model. Different locations in the network have the same pore and throat size. Therefore, it is easy to study the flow patterns due to local heterogeneity. Ma and Ruth (1993) used simple porous media (even periodic) to analyze the source of non-Darcy flow in Forchheimer equation.

## 3 Modeling

### 3.1 DNS calculations

The incompressible single-phase fluid flow through the geometries mentioned above is simulated by solving mass and momentum conservation equations under steady-state condition:

Mass balance equation:

$$\nabla \cdot \mathbf{V} = 0 \tag{3}$$

Momentum balance equation:

$$\mathbf{V} \cdot \nabla \mathbf{V} = -\frac{1}{\rho}\nabla p + \frac{\mu}{\rho}\nabla^2 \mathbf{V} \tag{4}$$

Here, $\mathbf{V} = u\mathbf{i} + w\mathbf{j}$ is the velocity vector, and $p$ is the local static pressure. Water is set as the working fluid with viscosity $\mu = 0.001$ Pa · s and density $\rho = 998$ kg/m$^3$. On fluid–solid interfaces, no-slip boundary condition is assumed ($\mathbf{V} = 0$). The network's top and bottom faces (Fig. 1a, c) are exposed to symmetry boundary conditions. A constant mass flow rate enters the inlet, and the outlet boundary is exposed to zero pressure. Uniform velocity profile upstream the

contraction half pore is considered to model fluid flow in an isolated FP.

Pressure and velocity in Eqs. (3) and (4) are solved for the pore spaces using the semiimplicit method for pressure-linked equations (SIMPLE) implemented using the commercial software Ansys Fluent. Steady-state convergence is achieved when the residual for each component of the velocity becomes less than $10^{-6}$. In this study, the quadratic mesh is used to divide the domain into computing elements.

## 3.2 Pore network simulation (PNS)

### 3.2.1 Basics of mass balance

2D networks of pores and throats are generated based on the geometries that are given in Fig. 1. Mass balance around each pore body $i$ requires that

$$\sum_j Q_{ij} = 0, \tag{5}$$

where $Q_{ij}$ is the mass flow rate entering (leaving) pore body $i$ and leaving (entering) the adjacent pore body $j$. The flow rate of each FP is proportional to the pressure drop along that segment. Assume the following equations are applicable for contraction–expansion section and throat section separately:

$$Q_{ij}^{\mathrm{C}} = \eta^{\mathrm{C}} \Delta P^{\mathrm{C}} \tag{6a}$$

$$Q_{ij}^{\mathrm{t}} = \eta^{\mathrm{t}} \Delta P^{\mathrm{t}} \tag{6b}$$

$$Q_{ij}^{\mathrm{E}} = \eta^{\mathrm{E}} \Delta P^{\mathrm{E}}, \tag{6c}$$

where $\eta^{\mathrm{E}}$, $\eta^{\mathrm{C}}$, and $\eta^{\mathrm{t}}$ are proportionality parameters for expansion, contraction, and throat segments, respectively. Note that $\Delta P$ is the pressure drop across each element of the FP.

Knowing that for flow through a single FP $Q_{ij}^{\mathrm{E}} = Q_{ij}^{\mathrm{t}} = Q_{ij}^{\mathrm{C}} = Q_{ij}$ and $\Delta P_{ij} = \Delta P^{\mathrm{E}} + \Delta P^{\mathrm{t}} + \Delta P^{\mathrm{C}}$ one has:

$$Q_{ij} = \left( \frac{1}{\eta^{\mathrm{E}}} + \frac{1}{\eta^{\mathrm{t}}} + \frac{1}{\eta^{\mathrm{C}}} \right)^{-1} \Delta P_{ij}. \tag{7}$$

Inserting Eq. (7) in Eq. (5), one has a set of algebraic equation (maybe non-linear) which must be solved simultaneously to calculate the pressure at each pore:

$$\overline{[A]}\ \overline{[P]} = \overline{[D]}, \tag{8}$$

where

$$A_{mn} = \begin{cases} \left( \frac{1}{\eta^{\mathrm{E}}} + \frac{1}{\eta^{\mathrm{t}}} + \frac{1}{\eta^{\mathrm{C}}} \right)_{mn}^{-1} & m \neq n \\ -\sum_n \left( \frac{1}{\eta^{\mathrm{E}}} + \frac{1}{\eta^{\mathrm{t}}} + \frac{1}{\eta^{\mathrm{C}}} \right)_{mn}^{-1} & m = n \end{cases}. \tag{9}$$

$P$ is a matrix for the pores' pressure, and $D$ is a matrix for the network's boundary conditions. Here, $\overline{[.]}$ denotes a column matrix ($n \times 1$) while $\overline{\overline{[.]}}$ represents a $n \times n$ matrix, where $n$ is the number of pore bodies.

### 3.2.2 Proportionality parameters at the microscale

We use the word "microscale" to describe FP's components, such as a throat, an expansion, or a contraction. Traditionally Hagen-Poiseuille (HP) equation describes flow, $Q_{ij}^{\mathrm{t}}$, throughout the throat so that:

$$\eta^{t} = \frac{\rho b d_{\mathrm{t}}^3}{12 \mu l_{\mathrm{t}}}, \tag{10}$$

where $b$ is the depth of the channels normal to the plane. Here, it is assumed that the flow is fully developed. However, this is not an appropriate assumption for short throats where the ratio of throat length to its width is not considerable. The effect of "vena contracta" at the throat entrance adds additional resistance to the fluid flow. As Kanda and Shimomukai (2009) stated, there is a significant difference between the wall and centerline pressure near the channel entrance, which contradicts the boundary layer theory assumptions (no pressure gradient normal to the main flow direction) (Kanda and Shimomukai 2009).

For the contraction and expansion sections, $\eta^{\mathrm{C}}$ and $\eta^{\mathrm{E}}$ are functions of pore geometry ($d_{\mathrm{t}}$ and $d_{\mathrm{R}}$), average velocity, and flow patterns (Veyskarami et al. 2016; El-Zehairy et al. 2019). Different correlations have been suggested yet for the contraction pressure drop. Kays submit the most comprehensive one in 1950. He analyzed the abrupt pressure drop between two long pipes of different diameters. Kays' correlation is limited to Reynolds numbers of the order $10^5$ and above (the Reynolds number is calculated based on the smaller bore size) (Bullen et al. 1987). Bullen et al. (1987) proposed a correlation for sudden contraction and suggested that the coefficient loss is mildly affected by the Reynolds number. Their correlation was reported for large Reynolds numbers ($\mathrm{Re} > 20 \times 10^3$). They examined the effect of edge sharpness and showed a considerable variation in the loss coefficient. Traditionally, the pressure drop in the contraction is predicted by

$$\left( \frac{\Delta P}{\rho v_{\mathrm{t}}^2} \right)^{\mathrm{C}} = \frac{1}{2} \left( 1 - \frac{1}{C_{\mathrm{c}}} \right)^2. \tag{11}$$

The contraction coefficient, $C_c$, is a function of $\sigma = \frac{d_t}{d_R}$ and Reynolds number. In the turbulent regime, the contracta effect becomes independent of Reynolds number (Bullen et al. 1987):

$$C_c = 1 - \frac{1-\sigma}{2.08(1-\sigma)+0.5371}. \quad (12)$$

Nevertheless, as is examined by Abdelall and coworkers (Chukwudozie and Tyagi 2013), Eq. (11) cannot accurately simulate the pressure loss in the laminar regime. Alternatively, the following relation is proposed for Re < 1000 (Chalfi and Ghiaasiaan 2008):

$$\left(\frac{\Delta P}{\rho v_t^2}\right)^C = 0.0294 \ln \mathrm{Re} + 0.0109 + \frac{1}{2}\left(1-\sigma^2\right). \quad (13)$$

In the mentioned studies, it is assumed that the flow approaching the contraction is fully developed. Disturbances are propagated upstream, which cause changes in the flow patterns at a point of approximately $4d_t$ upstream of the contraction. The fully developed flow is re-established approximately $4d_t$ -14 $d_t$ downstream from the contraction in the throat (Bullen et al. 1987). In all the above formulations for pressure drop in contractions, the vena contracta effect is included in the equation ($C_c$) and is known to be a function of flow regime and dimension (Bullen et al. 1987; Abdelall et al. 2005).

The dimensionless pressure gradient in the expansion section is cubic due to the boundary layer separation (White 2005). Its value is negligible compared with those of throat and contraction sections at small flow rates. An equation similar to Eq. (6c) is suggested in the literature for the sudden expansion of the fluid flow in the turbulent regime. The laminar regime's flow patterns is highly dependent on the Reynolds number, as is proved by different experiments. Chalfi and Ghiaasiaan (2008) proposed the following relation for sudden expansion in the laminar regime:

$$\left(\frac{\Delta P}{\rho v_t^2}\right)^E = \frac{1}{2}\left(\sigma^2-1\right) - 0.1077 + 0.0021\mathrm{Re} - 2.5\times10^{-6}\mathrm{Re}^2 \quad \mathrm{Re} < 400. \quad (14)$$

As far as we know, the equations introduced to predict pressure difference in contractions and expansions have parameters that must be obtained for each geometry. In real porous media, there is a variety in the shape and geometry of the pore bodies. If not impossible, it is very inefficient to find the constants for each geometry.

The method for calculating the pressure gradient in expansions and contractions is of significant importance. Due to the complicated flow regime in the area of size change, no accurate measurement is possible. Researchers calculate the pressure before and after the size change at some points far from it (where the flow is fully developed). Then the values are extrapolated to obtain two pseudo pressures at size change. The pressure difference is then calculated by subtracting these two pseudo pressures. However, this is not an appropriate method for porous media calculations where the developed flow between the obstacles is rarely occurred.

Some other relationships are also proposed for laminar flow through different converging/diverging capillaries (a FP) by other authors (Veyskarami et al. 2016,2018).

This study analyzes the fluid flow in different isolated FPs, including trapezoidal and circular half-pores, and calculates their pressure gradient using DNS. According to Fig. 1b, the geometric parameters affecting the permeability of an isolated FP at the microscale level are $d_t$, $l_t$, $d_R$ or $d_C$. The fluid and flow parameters are $\rho$, $\mu$, $\Delta P$. Since the throat velocity, $v_t$, has the least variations within a FP; we used it as the characteristic velocity. With these parameters, there are five sets of dimensionless groups, as suggested by the π-Buckingham method:

$$\left(\frac{\Delta P}{\rho v_t^2}\right)^t = f\left(L_t,\ \mathrm{Re},\ D_R \text{ or } D_C\right) \quad (15a)$$

$$\left(\frac{\Delta P}{\rho v_t^2}\right)^C = f\left(L_t,\ \mathrm{Re},\ D_R \text{ or } D_C\right) \quad (15b)$$

$$\left(\frac{\Delta P}{\rho v_t^2}\right)^E = f\left(L_t,\ \mathrm{Re},\ D_R \text{ or } D_C\right). \quad (15c)$$

Here, the characteristic geometrical parameter is the throat width $d_t$ and other aspect ratios are calculated as $L_t = l_t/d_t$, $D_R = d_R/d_t$, $D_C = d_C/d_t$ and $\mathrm{Re} = \frac{\rho v_t d_t}{\mu}$.

Upstream an isolated FP a uniform velocity profile is defined at the contraction section, and the pressure at any micro-segment is calculated. Appendix 1 describes the area-averaged method for calculating $P$ at each section of the FP.

## 4 Simulation results and discussion

### 4.1 Correlations for microscale proportionality parameters

We simulated fluid flow in different geometries at the microscale level for isolated FPs using DNS. To ensure that the results are independent of mesh size, we increased the mesh number and inspected the mesh dependency.

First, we studied the effect of each dimensionless parameter on $\frac{\Delta P}{\rho v_t^2}$ of segments. It was observed that $\left(\frac{\Delta P}{\rho v_t^2}\right)^t$ and $\left(\frac{\Delta P}{\rho v_t^2}\right)^C$ are not affected by their up and downstream geometries, while $\left(\frac{\Delta P}{\rho v_t^2}\right)^E$ is influenced by $L_t < 3.5$ up to 10%. This sensitivity is interpreted as follows. For small $L_t$, the flow in the throat is not fully developed when it enters the expansion section. Consequently, the velocity profile in the throat outlet still tends to reshape while entering an expansion.

Based on 82 datasets for $1 \le L_t \le 15$ and $0.001 \le \mathrm{Re} \le 265$, the following correlations are suggested in the throat:

$$\left(\frac{\Delta P}{\rho v_t^2}\right)^t = 8.753 L_t \mathrm{Re}^{-1} + 0.1289 \quad L_t \mathrm{Re}^{-1} \le 0.075 \tag{16a}$$

$$\left(\frac{\Delta P}{\rho v_t^2}\right)^t = 10.472 L_t \mathrm{Re}^{-1} \quad L_t \mathrm{Re}^{-1} > 0.075. \tag{16b}$$

Figure 2 compares Eq. (16) with DNS results. As is observed HP model $\left(\left(\frac{\Delta P}{\rho v_t^2}\right)^t = 12 L_t \mathrm{Re}^{-1}\right)$ differs from DNS results, especially for $\frac{L_t}{\mathrm{Re}} \le 0.075$ since the fully developed assumption fails at both ends of the throat. The absolute relative error is calculated as follows:

$$\%\text{Abs rel err} = \frac{\left|\left(\frac{\Delta P}{\rho v_t^2}\right)_{\mathrm{DNS}} - \left(\frac{\Delta P}{\rho v_t^2}\right)_{\mathrm{Model}}\right|}{\left|\left(\frac{\Delta P}{\rho v_t^2}\right)_{\mathrm{DNS}}\right|}. \tag{17}$$

The model predicts a maximum absolute error equal to 31.7%.

For the circular contraction section, the following relation is obtained by analyzing DNS data over 81 datasets:

$$\left(\frac{\Delta P}{\rho v_t^2}\right)_C^C = 2\left(4.61 D_C^{-1.51} + 1.891\right)/\mathrm{Re} - 0.418 D_C^{-2.04} + 0.5. \tag{18}$$

The maximum and average deviations for Eq. (18) are found to be 3.5% and 1.1%, respectively. In Fig. 3, DNS results for circular contraction segments are compared with Eq. (18) to show the model's accuracy. DNS data of trapezoidal pores are depicted for better comparison. Despite the excellent accuracy for circular pores, Eq. (18) fails to predict the hydraulic properties of trapezoidal half pore bodies. Instead, DNS data for trapezoidal pores fit suitably with the following correlation (over 70 datasets):

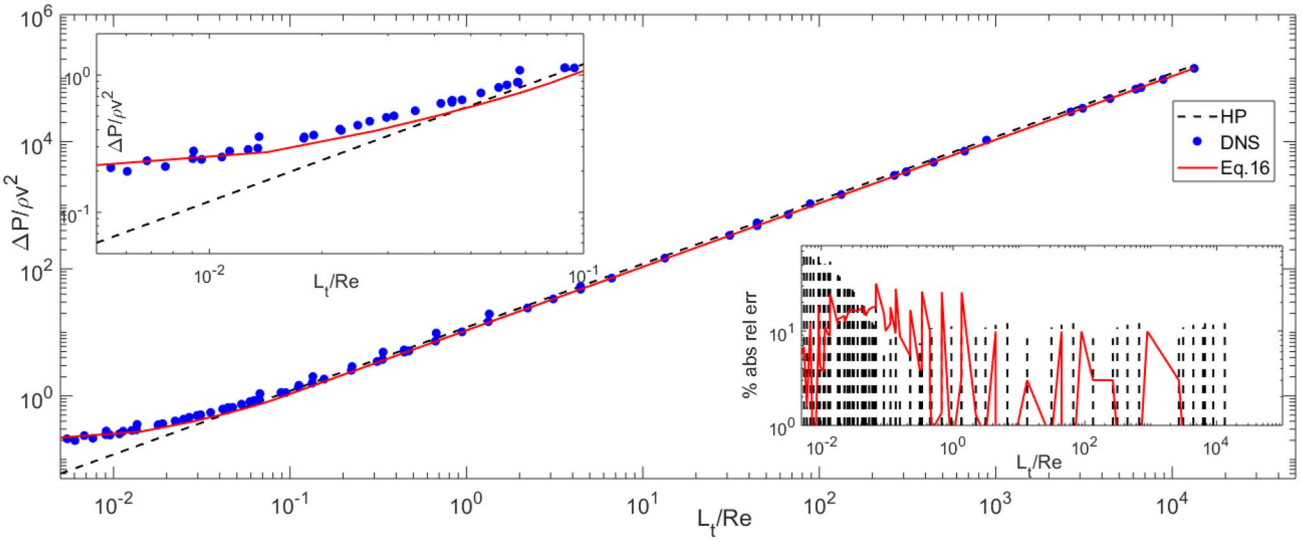


**Fig. 2** Dimensionless pressure drop in the throat versus $\frac{L_t}{\mathrm{Re}}$. The upper insect shows $\left(\frac{\Delta P}{\rho v_t^2}\right)$ versus $\frac{L_t}{\mathrm{Re}}$ for $\frac{L_t}{\mathrm{Re}} < 0.1$ and the lower one presents the absolute relative error

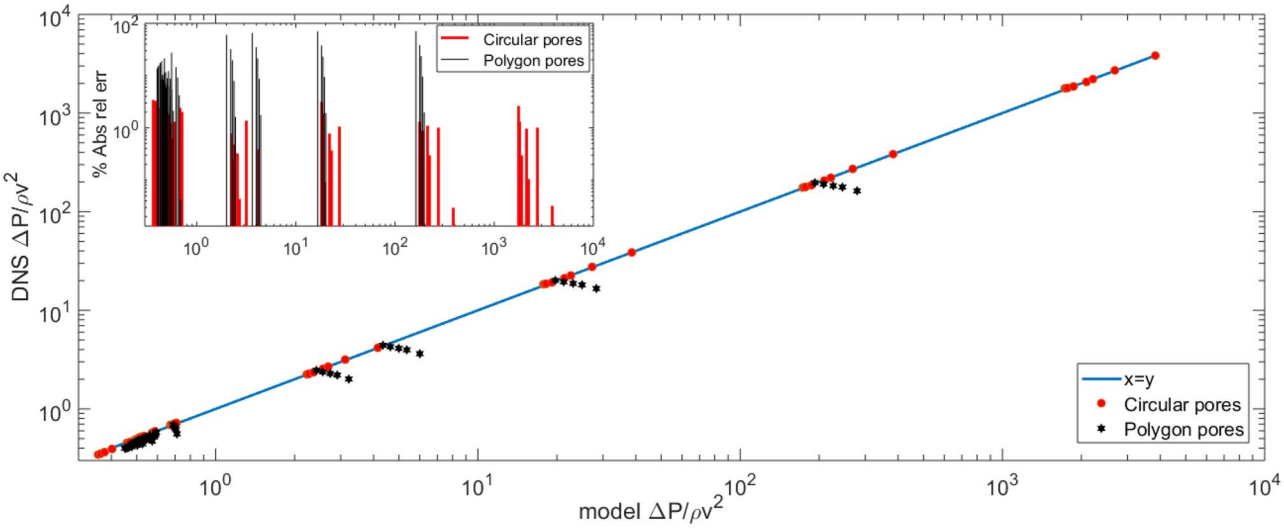


**Fig. 3** Dimensionless pressure drop for the contraction section calculated by DNS versus that predicted by Eq. (18). Inset shows the absolute relative error

$$\left(\frac{\Delta P}{\rho v_t^2}\right)_R^C = \left(-8.02 D_R^{-2.98} + 4.2\right)/\mathrm{Re} - 0.681 D_R^{-2.308} + 0.4772\,. \tag{19}$$

The maximum and average departure for Eq. (19) are 2.8% and 0.93%, respectively.

The preceding procedure was repeated for DNS data of the expansion section. As cited above, three parameters affect $\left(\frac{\Delta P}{\rho v_t^2}\right)_C^E$ say $L_t$, $D_C$ and Re. Considering several correlations, Eq. (20) was found to correlate the DNS data for circular pores with a considerable error as shown in Fig. 4 (with maximum and the average deviation of 914% and 47% over 362 datasets, respectively):

$$\left(\frac{\Delta P}{\rho v_t^2}\right)_C^E = -\frac{0.00367}{L_t} + \frac{0.0372}{D_C} + \frac{0.592}{\mathrm{Re}} - 4.9\exp\left(-0.93\mathrm{Re}\right). \tag{20}$$

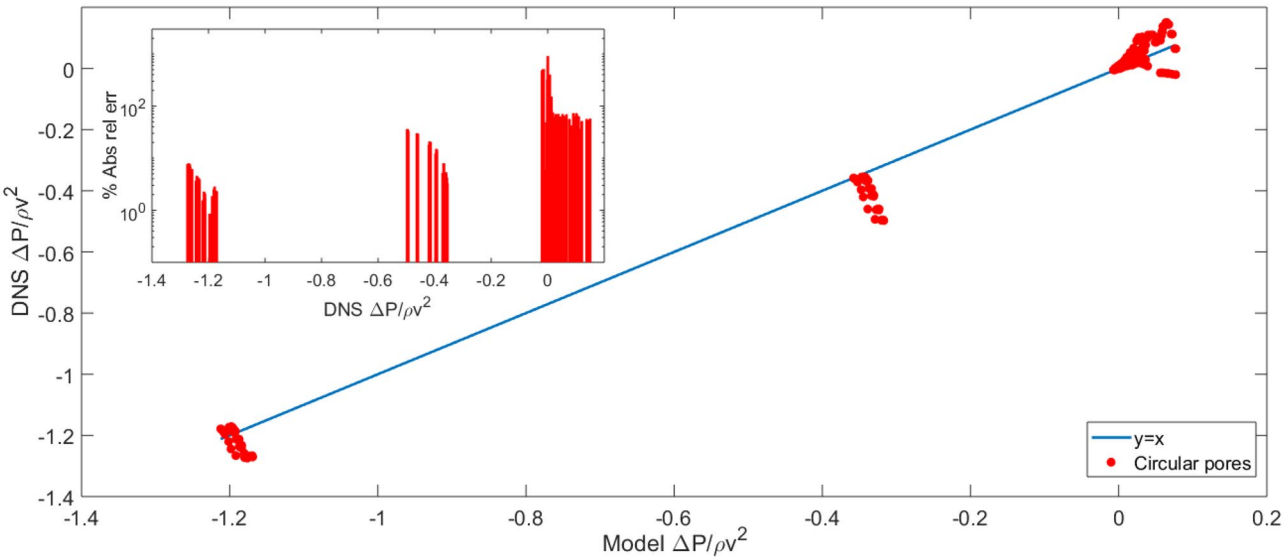


**Fig. 4** Dimensionless pressure drop for the circular expansion section calculated by DNS versus that predicted by Eq. (20). Inset shows the absolute relative error

Equation (20) could not accurately correlate DNS data for trapezoidal pores (because of substantial deviations, they are not indicated in Fig. 4). Instead, it was found that the following correlation can precisely simulate DNS data for trapezoidal pores with parameters tabulated in Table 1:

$$\left(\frac{\Delta P}{\rho v_{\mathrm{t}}^2}\right)_{\mathrm{R}}^{\mathrm{E}} = \frac{\left(p_1 \mathrm{Re}^3 + p_2 \mathrm{Re}^2 + p_3 \mathrm{Re} + p_4\right)}{\left(\mathrm{Re}^2 + p_5 \mathrm{Re} + p_6\right)}, \tag{21a}$$

where the coefficients $p_i$ are estimated by

$$p_i = \frac{a_1 D_{\mathrm{R}} + a_2}{D_{\mathrm{R}} + a_3}. \tag{21b}$$

Table 2 reports the coefficients $a_i$ for Eq. (21b). Note that as we used data in Table 1, the effect of $L_{\mathrm{t}}$ is not explicitly shown in the equation. Equation (21) correlates DNS data for trapezoidal pores with a maximum departure equal to 51.4% and an average deviation over 70 datasets equal to 17.46%. It is worthwhile to mention that the deviation decreases significantly for Reynolds numbers greater than 2.

In sum, the correlations are very sensitive to pores' shape, and using an incorrect pair of correlations in PNS may lead to inaccurate results.

## 4.2 Assessment of the correlations

This section assesses the exactness of correlations derived in Sect. 4.1. To this purpose, we selected a FP from the pore in series (Fig. 1c), and six FPs form different positions in Network 3, far from the inlet and the outlet of the network. The dimensionless pressure difference $\left(\frac{\Delta P}{\rho v_{\mathrm{t}}^2}\right)$ for each micro-segment is calculated using DNS and compared with the predictions of Eqs. (16), (19), and (21). The area-averaged formulation is used to calculate the pressure at each intersection (Appendix 1).

Figure 5 demonstrates the streamlines at six different positions within Network 3. Local heterogeneity influences the streamlines appreciably. Eddies likewise impress flow patterns in pore bodies and the subsequent flow elements. Whether PNS could consider these effects will be discussed in the following paragraphs.

As shown by Fig. 6, Eq. (16) can suitably resemble DNS data extracted from FPs in series, especially at elevated $\frac{L_{\mathrm{t}}}{\mathrm{Re}}$. DNS data from six different FPs in network 3 (as shown in Fig. 5) are also used to examine Eq. (16). While Eq. (16) fits most DNS data, data series 6 exhibits different behavior, particularly at higher Reynolds numbers. In series 6, there is a large angle between the throat axis and the streamlines upstream. In other words, throat 6 and streamlines in the upstream pore are not co-axial due to topology and flow patterns in the upstream pore. The mesh refining effect is presented in Fig. 6, which shows an excellent agreement with the extracted correlation. To this end, we refined the number of meshes from 6000#/m to 10,000#/m in isolated FP.

Figure 7 examines the accuracy of Eq. (21) for the expansion section. Except for low Reynolds numbers, DNS data from FP in series and Network 3 coincide with the trend predicted by Eq. (21). The main reason DNS data and correlation 21 are matched, especially at high Reynolds numbers, is jet-like flow at the center of the expansion section. At this condition, the shape of the pore body becomes less crucial. DNS data after mesh refining of isolated FP are shown, and it is evident that Eq. (21) is independent of the mesh size.

The results extracted from DNS data of Network 3 and FPs in series poorly follow the trend predicted by Eq. (19), as presented by Fig. 8. Nevertheless, the goodness of the correlation for series 2, 4, and 5 is notable. Moreover, Eq. (19) can well represent the mesh-refined data of isolated FP.

It is interesting to compare the magnitude of pressure difference in contraction and expansion segments at the same Reynolds number: the pressure difference in an expansion segment is negligible compared with a contraction one in large Reynolds numbers.

To further explore the flow field in FP, we probed the streamlines of an isolated FP (Fig. 9), FPs in series (Fig. 10), and FPs in a network 3 (Fig. 11).

Figure 9 show that streamlines are approximately parallel and converge following the contraction section's geometry. Eddies appear as a consequence of flow separation downstream the expansion section. They get larger as the velocity increases until the head of the eddy reaches the throat outlet. A large portion of the fluid passes through the expansion center at high velocities, known as streamlining or inertial core flow (Newman and Yin 2013). No inertial core flow is observed in the contraction section due to the defined boundary condition. It is worth reminding that these simulations were used to derive the correlations in Sect. 4.1.

With this background, one expects that the eddies downstream of an expansion segment influence the flow patterns

**Table 2** Parameters $a_i$ for Eq. (21b) according to the geometries described in Table 1

| | $p_1$ | $p_2$ | $p_3$ | $p_4$ | $p_5$ | $p_6$ |
|---|---|---|---|---|---|---|
| $a_1$ | 0.001718 | –0.3767 | 20.29 | 86.06 | –40.94 | –0.001107 |
| $a_2$ | –0.002844 | 0.6539 | –35.02 | –142.3 | 55.4 | 0.00195 |
| $a_3$ | –0.5757 | –0.5223 | 0.6677 | –0.9698 | 0.6711 | 0 |

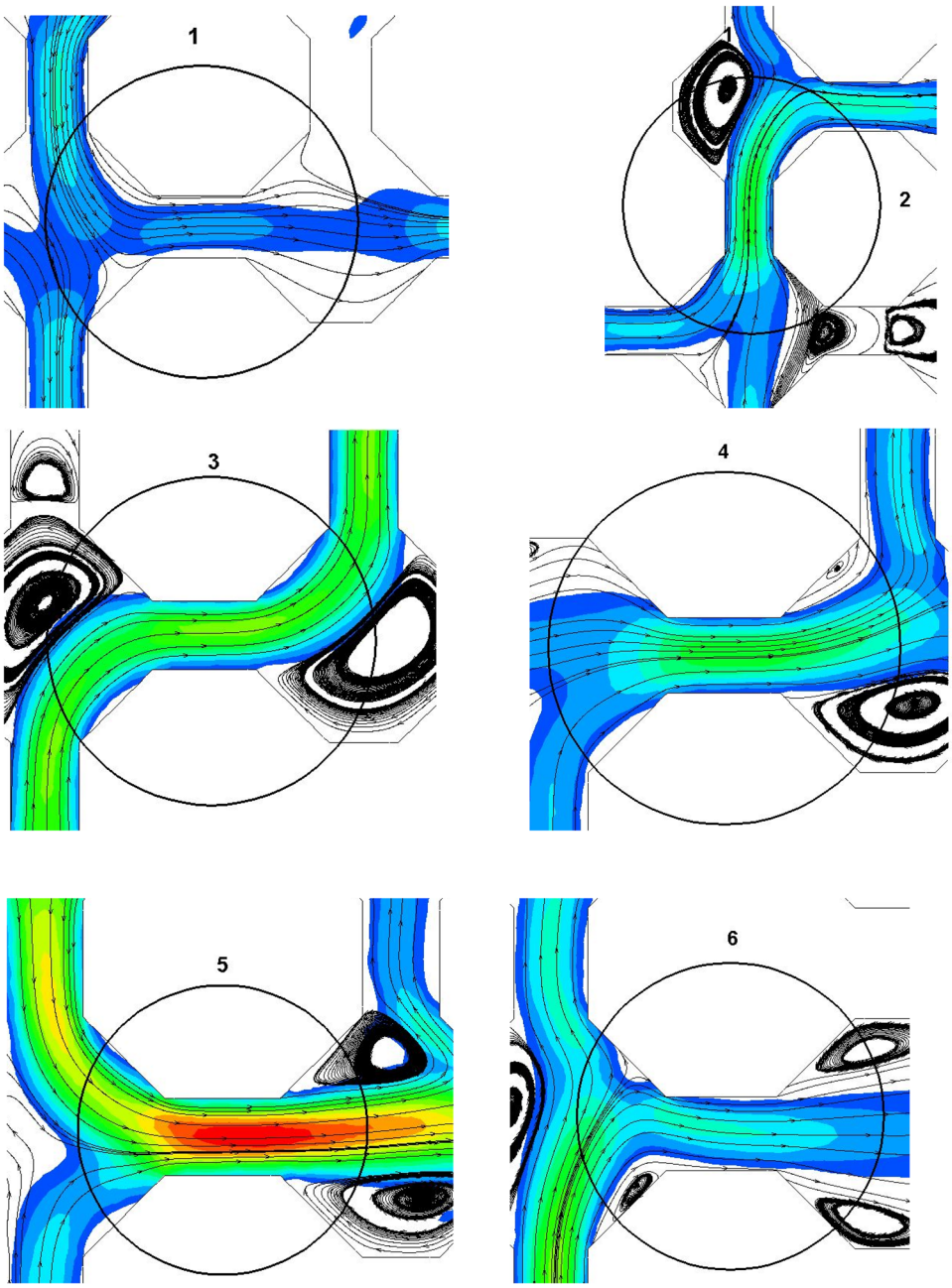


**Fig. 5** Different FPs in Network 3 used to validate Eqs. (16), (19), and (21). Contours display velocity. Hot colors are higher in velocity, cooler's are lower in velocity

in contraction section in a network. This phenomenon is observed in Fig. 10 for FP in series. Note that the lower boundary is exposed to symmetry boundary condition (see Fig. 1c) and has no effective flow rate. Besides, the shape of the eddies is noticeable. Steady small eddies are detectable at $\rho U/\mu = 800$ $(\mathrm{m}^{-1})$, and their size increases with an increase in the superficial velocity. Appendix 2 describes the method we used to detect the eddies. The head of the eddy begins in the expansion section, and as the velocity increases, the tail extends into the contraction section. Tails disturb the flow patterns, occupy the pore body, and reduce the flow-section.

As a consequence of large eddies, the core flow enters the contraction section. When the fluid does not experience the walls of contraction section, the pressure loss reduces, as shown in Fig. 8. It is in contrast with the uniform boundary condition applied to obtain Eqs. (18) and (19). Comparing Fig. 9 with Fig. 10 shows that eddies can be detected at a lower velocity (in FP in series) than they form in isolated FP. It is attributed to the existence of obstacles downstream of an expansion, which causes reverse flow. That means inertia effects start earlier than was expected from isolated FP.

Figure 11 represents the streamlines in a portion of network 3 at different velocities and emphasizes some

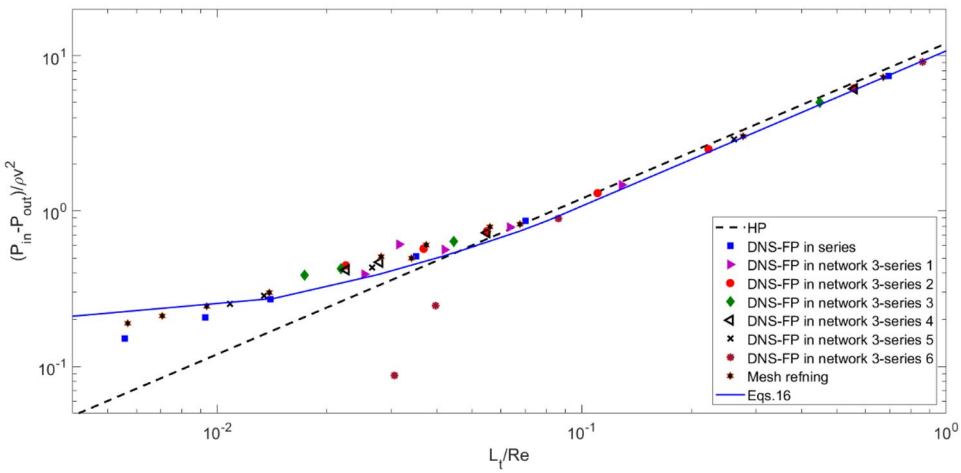


**Fig. 6** Comparison between the model prediction and DNS data of throats

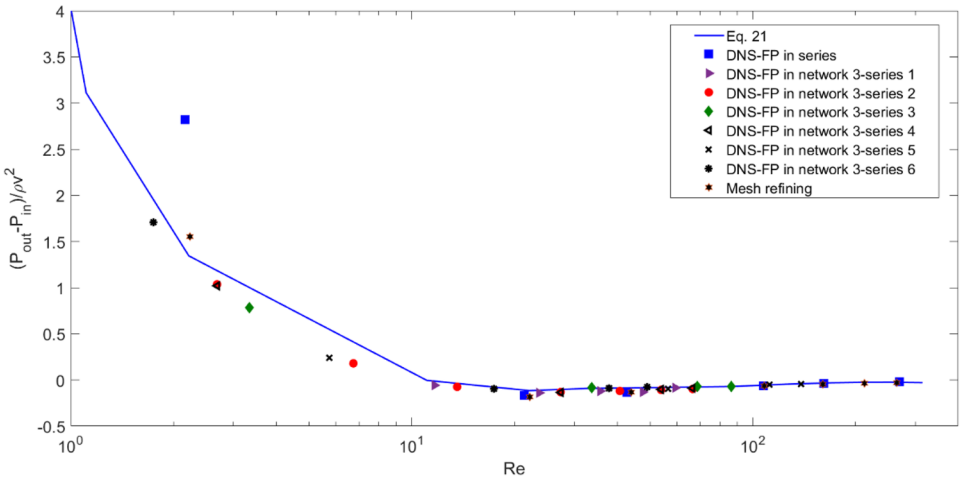


**Fig. 7** Comparison between the model prediction and DNS data of the expansion section

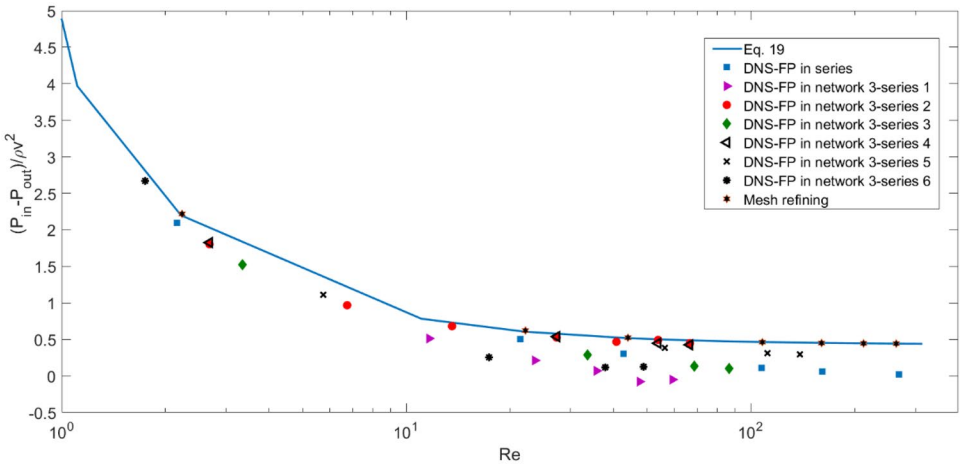


**Fig. 8** Comparison between the model prediction and DNS data of the contraction section

differences between flow in isolated FP and FPs in a network using five numbers.

Generally, at lower fluid velocity, the flow can spread over the pore body showing the significance of shear flow compared with inertia flow. By increasing the velocity, the fluid has less tendency to reshape because of inertia. Strictly speaking, the following deviations are observed in comparison with isolated FP:

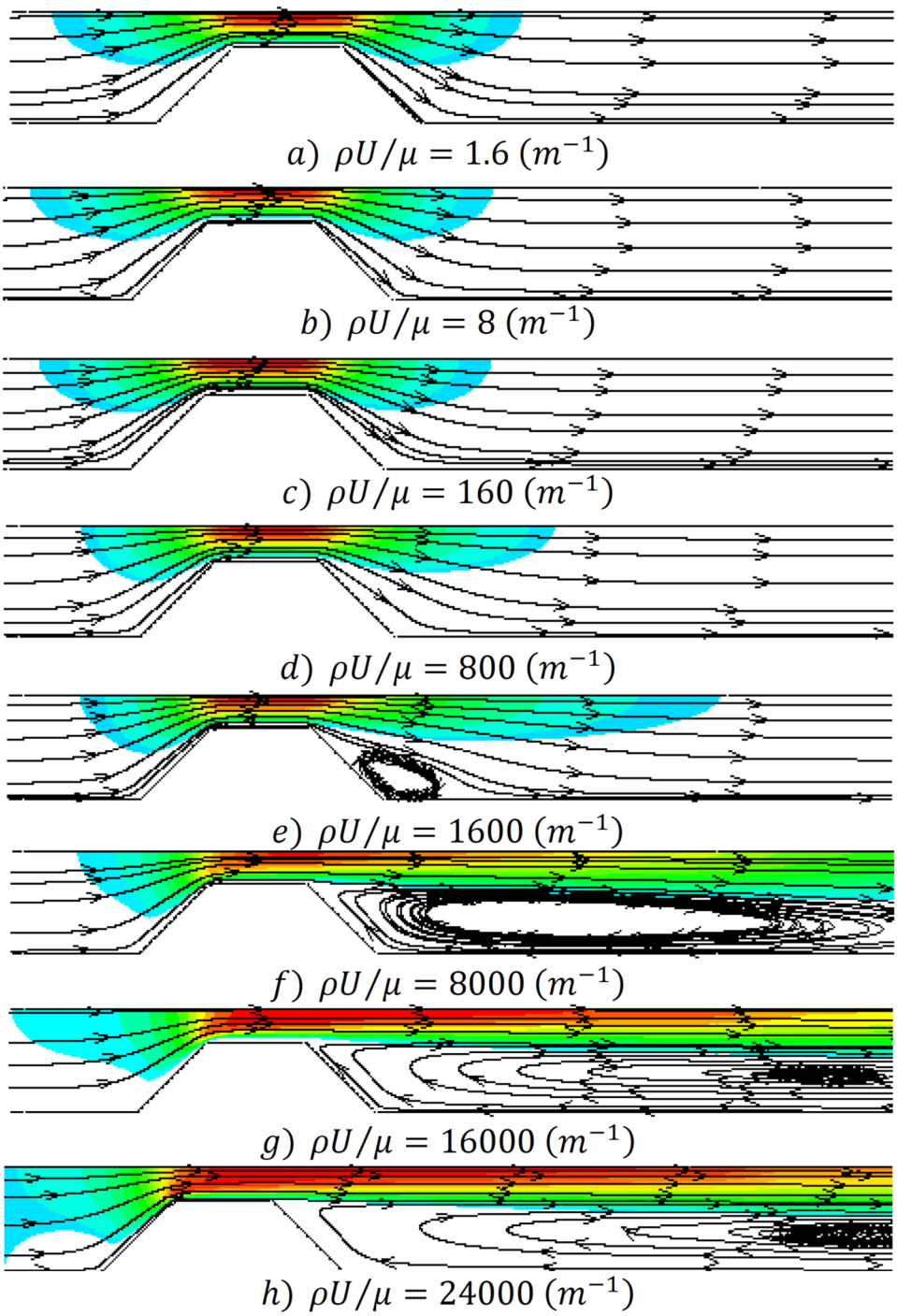


**Fig. 9** Streamlines and velocity contours for fluid flow in isolated FPs. Hot colors are higher in velocity, cooler's are lower velocity

- Differences in the shape of the streamlines entering the contraction due to eddies, bending, and topology (# 1);
- Inertial core at expansion outlet (# 2);
- Asymmetric flow at contraction inlet (# 3 and # 4);
- Asymmetric flow patterns at expansion outlet due to bending (# 4 and # 5);
- Deviation of flow to the corner of the pore body because of differences in momentum (# 1 and # 5).

To the best of our knowledge, none of these phenomena is considered in the aforementioned correlations or the literature. An interesting phenomenon is the formation of eddies at the entrance of the throat. As depicted by circles in Fig. 11g, the fluid bypasses other open throats to find less resistant paths.

Let us consider Fig. 5 again. The flow patterns entering the contraction sections in series 2, 4, and 5, are very similar

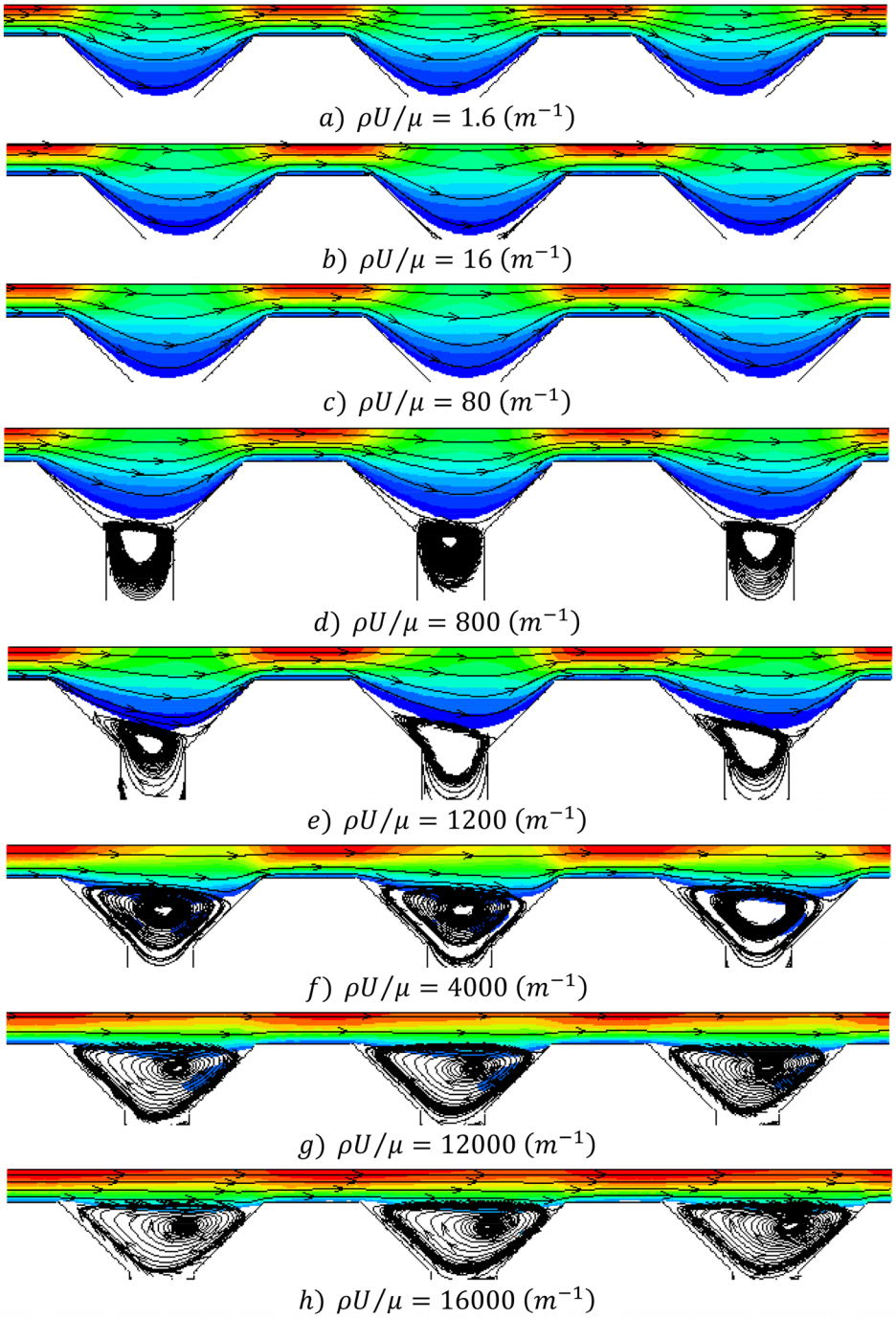


**Fig. 10** Streamlines and velocity contours for fluid flow in periodic FPs. Hot colors are higher in velocity, cooler's are lower velocity

to those observed at the contraction section in isolated FP (Fig. 9). Therefore, a minimum deviation between correlation 19 and DNS data is expected, as asserted by Fig. 8. By contrast, deviations in data series 1, 3, and 6 of Fig. 5 are attributed to differences between the flow patterns of isolated FP and FP in a network at the contraction section. Therefore, one expects that eddies in Network 3 are formed at a lower velocity than FP in series. Figure 11e shows that eddies can be detected visually at $\rho U/\mu = 415\ \ (\mathrm{m}^{-1})$ (see the criteria that are discussed in Appendix 2). Here, $U = Q/\rho A_{\mathrm{Network}}$ is the superficial velocity, and $A_{\mathrm{Network}}$ is the area of the network perpendicular to the main flow direction.

Figure 12 reports inverse apparent permeability ($K_{\mathrm{app}}^{-1} = \Delta P/L\mu U$) for FP in series calculated by DNS and PNS. First, the HP model accompanied by Eqs. (19) and (21) for contraction and expansion sections were used. Then, Eqs. (16), (19), and (21) were employed in PNS.

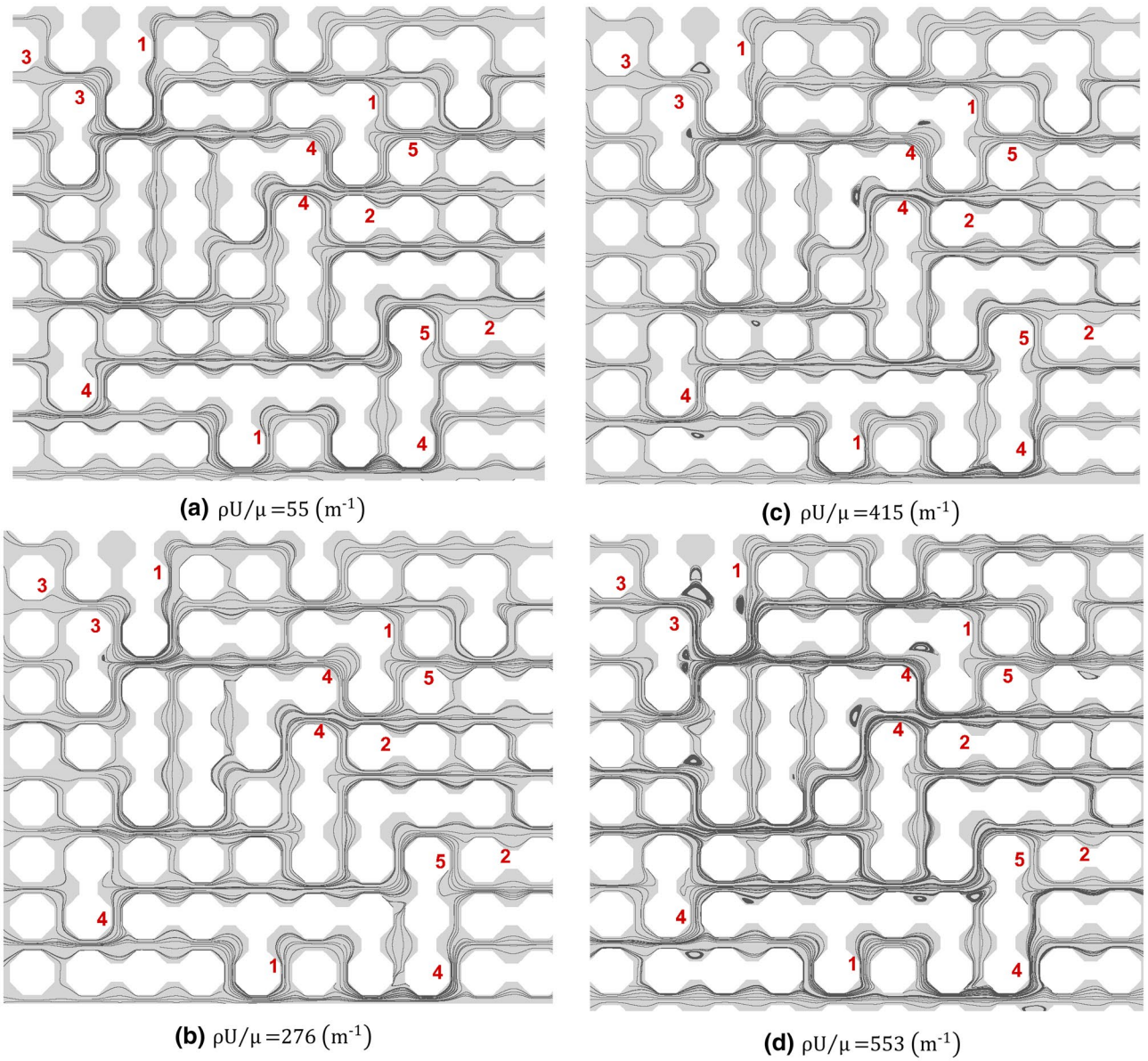


**Fig. 11** Streamlines for fluid flow in Network 3. Numbers are used to emphasizing the differences with isolated FP as explained in the text

The trends in Fig. 12 shows that Eq. (16) is somewhat more reasonable. Note that the differences between PNS and DNS data are mostly assigned to the inadequacy of Eq. (19) in simulating core flow. We marked the point where the smallest eddies are seen in the pore body. As pointed out before, eddies form in isolated FP at higher superficial velocities.

Figure 12 also shows the resistance of each segment against the fluid flow in the network (See Appendix 3). Evidently, the throat and contraction sections together have the primary resistance against flow transfer. The effect of the expansion section can be ignored, as suggested by Eq. (19).

PNS over predicts the apparent permeability at lower velocities and under predicts that at the higher ones. Figure 7 expressed that the expansion model is inaccurate at lower velocities. With inertial core flow at higher velocities, less portion of the fluid experiences the pores' walls, leading to fewer shear stresses. Due to the periodic nature of FPs in series, pressure drag and viscous drag on the solid walls control the pressure loss on every single FP in the system. It can be claimed that eddies formed in pore bodies cause adverse pressure gradients that decrease the pressure and viscous drag.

Eddies have just minor impacts on the total viscous dissipation. PNS does not account for the pressure loss due to

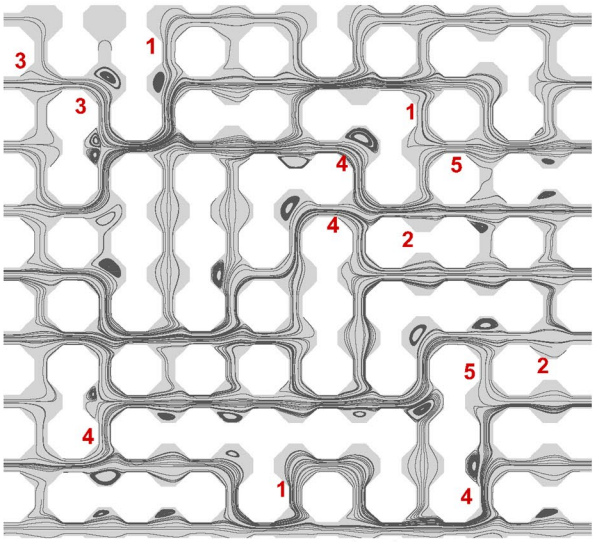

**(e)** $\rho U/\mu = 830\ (m^{-1})$

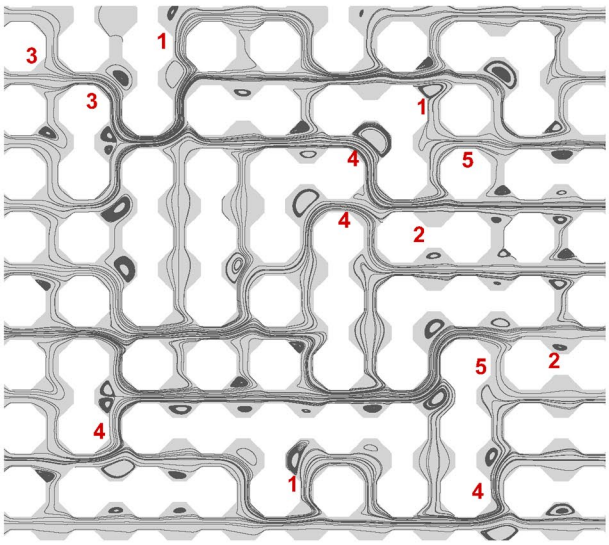

**(f)** $\rho U/\mu = 1660\ (m^{-1})$

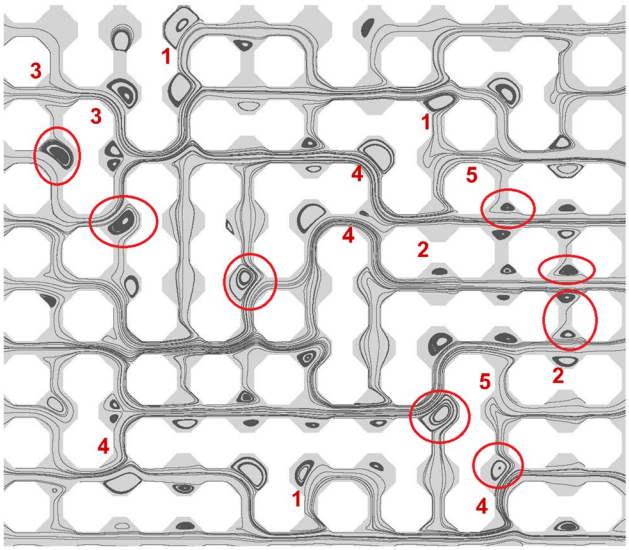

**(g)** $\rho U/\mu = 2765\ (m^{-1})$

**Fig. 11** (continued)

core flow (fluid–fluid interaction) in the contraction section. In contrast, the correlation for the contraction section inherently assumes that the fluid entering an isolated FP touches the pore walls entirely at the contraction section.

### 4.3 Pore network simulation

This section assesses PNS, equipped with the correlations obtained in previous sections, and compares the results with those of DNS in networks of octagon obstacles, as drawn schematically in Fig. 1a. For each geometry, the inlet flow rate varies, and the pressure drop over the entire network is calculated. Figure 13 displays the apparent permeability for different networks. As can be seen, the apparent permeability increases drastically with an increase in throat diameter.

The number of grids on each wall was increased from 10 to 30 to check the mesh independence. Due to limitations in computational facilities, more refinement was not applicable. Figure 14 exhibits the effect of mesh refinement for Network 3 at the maximum studied flow rate. No substantial change in the pressure drop is achieved by increasing the number of nodes above 25. Another interesting factor in studying mesh independence is analyzing the rate of dissipation of energy in the fluid due to internal viscous forces. Theoretically, the rate of viscous dissipation is proportional to $\Delta p$ over the entire network (Fourar et al. 2004; Talon et al.2012; Raeini et al. 2014):

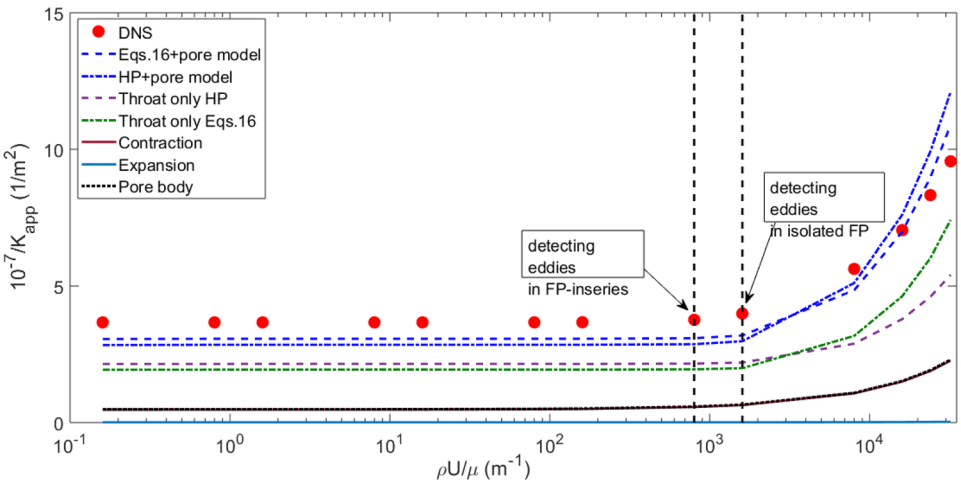


**Fig. 12** Inverse apparent permeability computed by DNS and PNS for FP in series

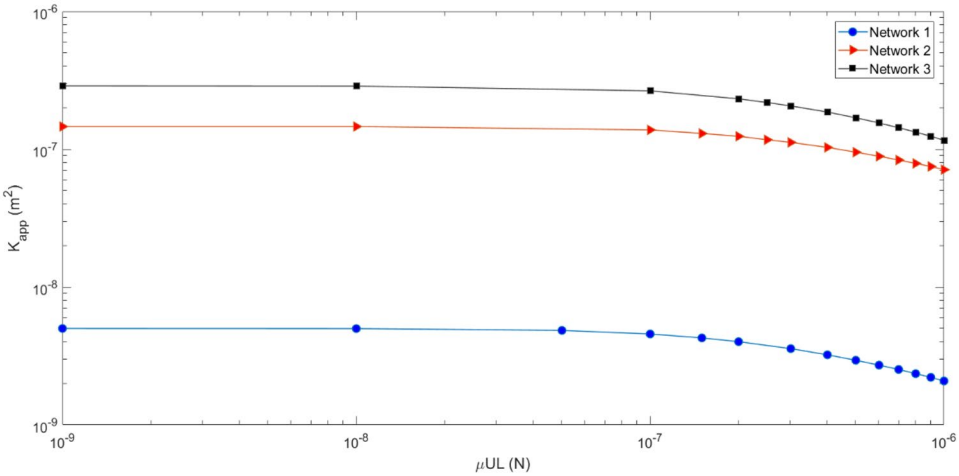


**Fig. 13** DNS obtained from different networks. Lines are drawn to aid the eye

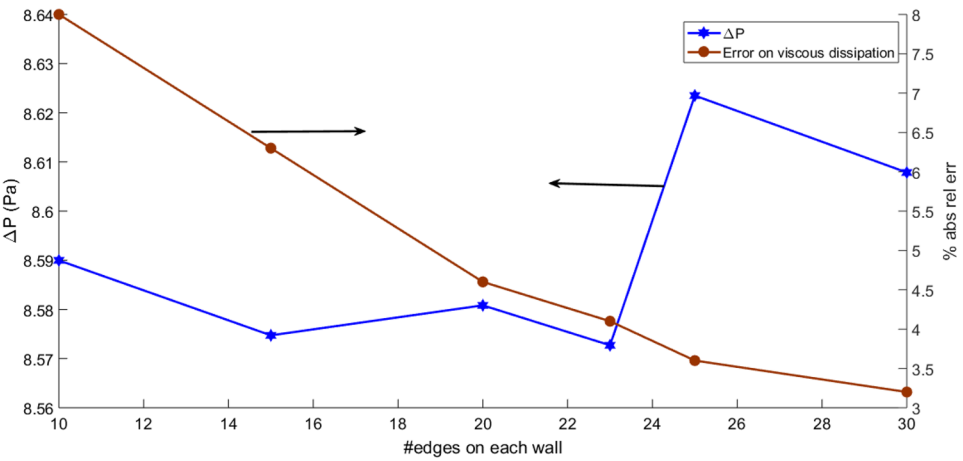


**Fig. 14** Mesh analysis for Network 3 at the maximum studied flowrate

$$Q\Delta P = \rho \int \varphi \mathrm{d}v, \tag{22}$$

where $\varphi$ is the energy dissipation, and d$v$ is the volume of each computing element. Integration is performed over all the fluid domain. Figure 14 also shows how this equality is accomplished as the mesh is refined. In this study, we used the normal ($F_n$) and tangential ($F_t$) forces in the flow direction to calculate the pressure drop in the Networks 1–3 ($\Delta P = \left(F_n + F_t\right)/A_{\text{Network}}$).

Different schemes for calculating pressure drop in the system are discussed elsewhere, and it is shown that they approximately give the same results (Raeini et al. 2014). However, Fig. 14 shows the dependency of the viscous dissipations algorithm (Eq. 22) on the grid number. Such dependency would be a significant problem in resolving the fluid flow in materials with too thin pores or networks of high heterogeneity.

Figure 15 compares PNS simulation results with DNS for different networks. Throat correlations (HP model and Eqs. 16) accompanied by pore side equations (Eqs. 19 and 21) are shown separately. The pore body and throat section's contributions to permeability are also drawn (Appendix 3). In all figures, we marked the point where eddies are detectable (Appendix 2). As was expected, the eddies appear at a lower superficial velocity in Network 3 than those observed in Fig. 12. Eddies form still at a lower velocity in Network 1 with $D_R = 9.48$. Eddy is likely to occur in systems with the most contrast between throats and pore sizes (Newman and Yin 2013). This event influences the cessation of the Darcy equation as well.

Regarding the difference in geometry between Network 2 ($D_R = 3.82$) and Network 3 ($D_R = 3.12$), one may expect that eddies should be found earlier in Network 2 than 3. However, this is in contradiction with what is observed. For further study, we calculated the tortuosity of the networks as (Koponen et al. 1996):

$$T = \frac{\langle \mathbf{V} \rangle}{\langle u \rangle}, \tag{23}$$

where $\langle \mathbf{V} \rangle$ is the average magnitude of the intrinsic velocity over the entire network area, and $\langle u \rangle$ is the average of its component along the main flow direction. It can be seen that the tortuosity of Network 2 is lower than that of Networks 1 and 3. From the viewpoint of mathematics, a larger tortuosity means a larger portion of fluid transporting perpendicular to the main flow direction. Therefore, the fluid in Network 3 encounters more obstacles rather than Network 2, leading to form larger eddies at a lower velocity. It can be concluded here that the local heterogeneity in the networks (despite equal mean connectivity) are essential in analyzing the flow patterns (Aramideh et al. 2018).

The criterion for the onset of non-Darcy flow in this study is the point where $\frac{K_{app}}{K_D} = 0.99$. Comparing Fig. 10d (formation of eddy) with Fig. 10e (cessation of Darcy equation), it can be inferred that non-Darcy flow initiates when eddies grow up and continue to fill the contraction section.

*Throat resistance*: As indicated in Fig. 15, throat resistance plays the most central role against the fluid's permeation. In Network 1 the magnitude of pore resistance is about one-tenth of the throat resistance. Therefore, any uncertainty in predicting flow patterns in pores is insignificant. Increasing the size of the pore bodies enhances their relative importance as well. Evidently, Eq. (16) is more reliable than the traditional HP equation.

*Combined pore-throat resistance*: Increasing width of the throats in networks postpones the onset of core flow, and increases viscous effect in the pore body. This effect is simulated by Eq. (19) and, and to some extent, by Eq. (21). As explained in the preceding paragraphs, the importance of flow patterns in the pore body becomes noteworthy when the pore size is comparable to the throat size (Networks 2 and 3). Half-pore correlations do not forecast the asymmetric flow patterns due to bending, branching, and eddies in networks with less open throats. These phenomena have convoluted, mostly unknown, impacts on fluid flow. For example, eddies cause viscous energy dissipation. They may lead the fluid to choose the shortest path, on the other hand. The majority of bending and branching is another anonymous phenomenon in PNS. Therefore, the inaccuracy of PNS results in Fig. 15 is assigned to the contribution of pore body in total permeability: with decreasing $D_R$, the importance of pore contribution to total resistance increases. Meanwhile, the contraction resistance predicted by Eq. (19) is not accurate enough in simulating such complicated flow. It can roughly be estimated here that the influence of eddies, branching, splitting, and core flow is much stronger than the contribution of fluid–solid as is considered in PNS (shear stresses in contraction section). PNS predicts negligible relative resistance of the expansion section for all three networks compared to the throat and the contraction segments.

Our findings are in agreement with the results of El-Zehairy et al. (2019) who simulated the fluid flow in four different natural and synthetic porous media using PNS and the correlations introduced by Kays. They compared their simulations with the results obtained by DNS (Muljadi 2016) and experimental data. Bentheimer and Estaillades sandstones have approximately the same topological characteristics with coordination numbers of 4.5 and 3.4, respectively, and can be compared according to morphological properties. Nevertheless, the porous media they studied have broad pore and throat size distributions. Suppose one uses the average pore and throat size as the representative for all morphological data. In that case, one has D = 1.893 and 1.69 for Bentheimer and Estaillades, respectively, where $D$ is the ratio of pore size to throat size. The results obtained in El-Zehairy et al. (2019) show that PNS underestimates the permeability for Bentheimer while it over predicts the permeability for Estaillades. Again for beadpack with D = 2, PNS underestimates DNS data. This is in line with the findings in the previous paragraph that increasing $D_R$ leads to overpredicting the permeability if one uses PNS.

Darcy permeability ($K_D$) is calculated by plotting the product $\mu U$ v.s. the pressure gradient $\left(\frac{\Delta P}{L}\right)$ near the zero

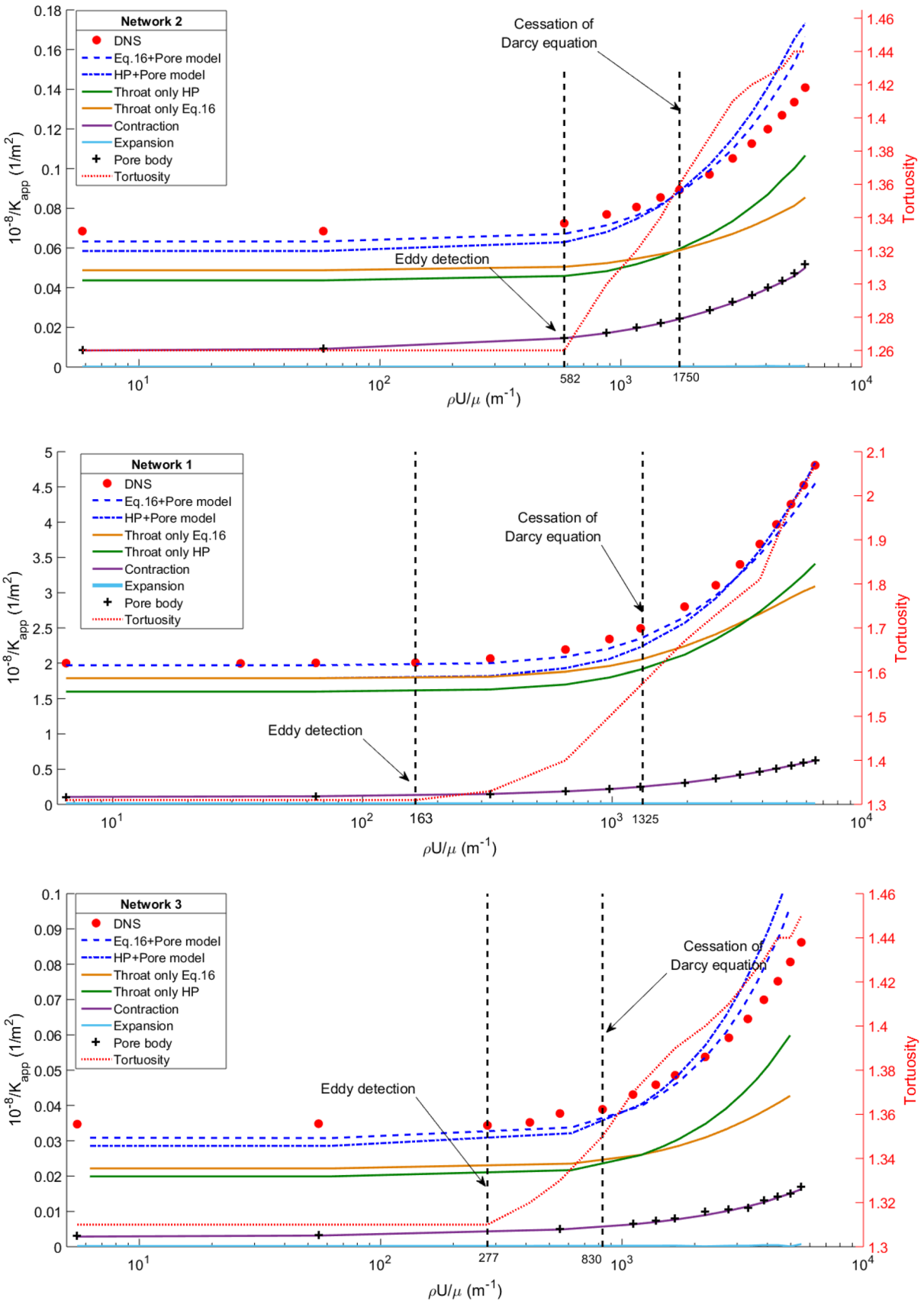


**Fig. 15** PNS results for networks 1–3 as compared with DNS data

velocity. The slope of the depicted line is reported as the Darcy permeability factor. At high velocities, the apparent permeability ($K_{app}$) of the system is predicted by Forchheimer equation as follows:

$$\frac{\Delta P}{L\mu U} = \frac{1}{K_{app}} = \frac{1}{K_F} + \beta\frac{\rho U}{\mu}, \tag{24}$$

where$\beta$ factor is deduced from the slope of the Forchheimer graph in the non-Darcy regime. Table 3 conveys $K_D$, $K_F$, and $\beta$ for different structures used in this work. Table 3 shows that PNS using the correlations mentioned above is not consistent unless for Network 1 where throat resistance controls $\Delta P$. The inaccuracy in predicting the Forchheimer coefficient ($\beta$) is more remarkable.

Some authors have recently started a new approach to benefit PNS and DNS's strengths simultaneously (Valvatne and Blunt 2004; Miao et al. 2017; Rabbani and Babaei 2019; Costa et al. 2018). They extracted the throats from tomography images modeled fluid flow in throats independently to find correlations for the throats' pressure drop. The boundary condition at these extracted throats is either uniform pressure or fully developed velocity. According to the findings in this study, these methods are reliable in Darcy flow merely, where viscous forces are dominant.

## 5 Conclusion

This article focuses on the exactness of PNS in estimating the permeability of 2D networks. Fluid passes over matrices of regularly arranged octagons. Each flow path consists of two half-pore bodies with a trapezoidal shape connected to a throat. The correct permeability is calculated by solving continuity and momentum equations using DNS. Appropriate correlations for pressure drop in each element of an FP are introduced and utilized in PNS. At the next step, we investigate the permeability data computed by PNS and DNS methods.

The following conclusions are drawn:

- The equations introduced in the literature for flow in expansions and contractions are mostly extracted for turbulent flow, and utilizing them in laminar flow is not justified. Most of them are not functions of the Reynolds number. In addition, they are extracted for some limited geometries.
- DNS data of isolated FPs do not justify the Hagen–Poiseuille equation. The developed flow criterion to derive the HP model is inexact for short wide throats.

**Table 3** Darcy and Forchheimer parameters extracted from DNS and PNS

| Domain name | | DNS | | | HP + Eq. (19) + Eq. (21) | | | Eq. (16) + Eq. (19) + Eq. (21) | | |
|---|---|---|---|---|---|---|---|---|---|---|
| | | $K_D \times 10^9$ (m$^2$) | $10^{-6}/K_F$ (m$^{-2}$) | $B \times 10^2$ (m$^{-1}$) | $K_D \times 10^9$ (m$^2$) | $10^{-6}/K_F$ (m$^{-2}$) | $\beta \times 10^2$ (m$^{-1}$) | $K_D \times 10^9$ (m$^2$) | $10^{-6}/K_F$ (m$^{-2}$) | $\beta \times 10^2$ (m$^{-1}$) |
| 1 | $L_t/d_t = 6/1;23\%$ | 4.17 | 197 | 437 | 4.7 (12.7%) | 147 (25.4%) | 530 (21.3%) | 4.4 (5.5%) | 189 (4.1%) | 397 (9.2%) |
| 2 | $L_t/d_t = 6/3;23\%$ | 132 | 6.92 | 12.6 | 150 (13.6%) | 3.6 (47.9%) | 29.9 (137.3%) | 142 (7.5%) | 4.3 (37.8%) | 24.3 (92.8%) |
| 3 | $L_t/d_t = 6/4;23\%$ | 237 | 3.23 | 9.69 | 258 (8.8%) | 1.45 (55.1%) | 20.43 (110.8%) | 258 (8.8%) | 2 (38.1%) | 15.2 (56.8%) |

Data in parentheses show relative absolute errors concerning DNS results

- Correlations used to model pressure drop in circular pores (contraction or expansion) are seldom applicable to trapezoidal pore bodies.
- Analyzing the fluid flow in a selected FP in a periodic porous medium (FPs in series) shows that the correlations can reasonably simulate the flow in the throats and the expansion sections. For the contraction section, the correlation failed to stimulate pressure loss. Investigating some selected FPs at different locations of the random network results in the same conclusion.
- We have examined the fluid streamlines in three different modes, i.e., isolated FP, FPs in series, and 2D pore networks. This examination uncovers the differences between correlations and single FP as follows:
- Downstream an expansion half pore, eddies form due to flow separation at high velocities, inducing the inertial core flow. This phenomenon is observed for a FP, isolated, or in a network.
- The tail of eddies may extend into the contraction half-pore section. Moreover, the upstream inertial core flow may enter the downstream throat without being affected by the contraction walls. Eddies might change the direction of streamlines compared with the isolated FPs.
- For isolated FP, the inlet flow to the contraction section is nearly flat (uniform flow) defined by the boundary conditions. However, an FP situation in periodic geometry or an FP in a network is quite different. The contraction section is affected by its upstream flow.
- Topology and flow patterns in the pore upstream a throat set the boundary conditions of that throat. It means that short-range correlations are important in modeling fluid flow in porous media at microscale.
- Due to the deviations explained mainly in the contraction section, PNS cannot accurately simulate DNS permeability data. However, if the contribution of throat resistance is much higher than the pore body resistance, PNS is reliable.

## Appendix 1: Pressure Profile in a FP

Figure 16 depicts the pressure profile in a single isolated FP. The average pressure at the inlet and outlet boundaries of each section are calculated using Eq. (25) and shown in the figure:

$$P(x) = \frac{1}{d}\int_0^d p(x,y)\mathrm{d}y. \tag{25}$$

In this equation, $d$ is the width of the FP perpendicular to $x$-direction ($d_t$ or $d_R$).

## Appendix 2: Eddy identification

To have a clearer picture of the number of eddies and how they affect the micro and macro flow, it is more convenient to compare the vortices' core and boundary directly. Here, we used the vortex identification method (Graftieaux et al. 2001; Epps 2017; Lahooti and Kim 2019), in which two scalars $\Gamma_1$ and $\Gamma_2$ indicate the core and boundary of the vortices, respectively. These scalars are computed as follows:

$$\Gamma_1(\boldsymbol{x}_P) = \frac{1}{N}\sum_s \frac{[\boldsymbol{r}_{PM}\times v_M]\cdot \boldsymbol{n}}{|\boldsymbol{r}_{PM}|.|v_M|} \tag{26}$$

$$\Gamma_2(\boldsymbol{x}_P) = \frac{1}{N}\sum_s \frac{[\boldsymbol{r}_{PM}\times (\mathbf{v}_M-\mathbf{v}_P)]\cdot \boldsymbol{n}}{|\boldsymbol{r}_{PM}|.|v_M-v_P|}. \tag{27}$$

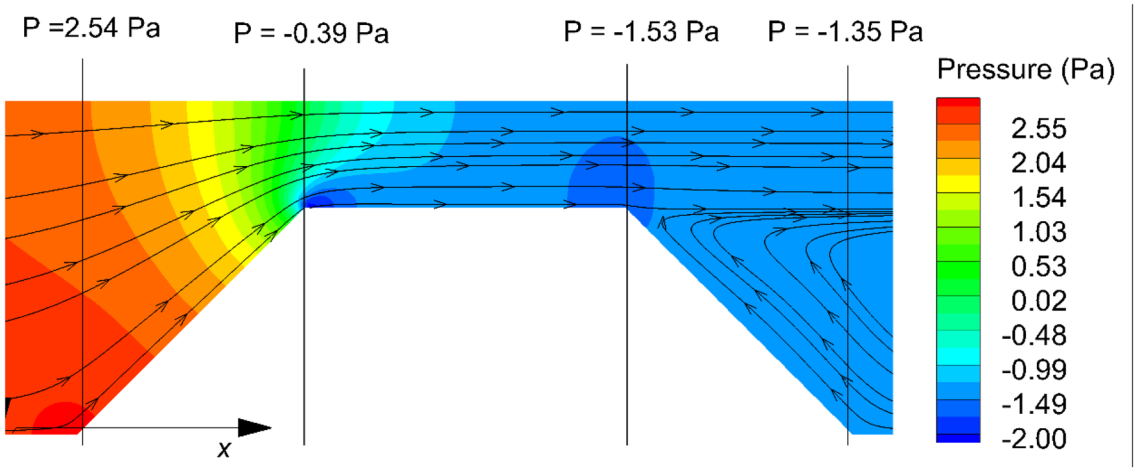


**Fig. 16** Pressure profile in an isolated FP and the associated averaged pressure

For any arbitrary point $\boldsymbol{x}_P$ in the computing domain, we defined an area **s** of $10\times10$ grid points surrounding $\boldsymbol{x}_P$, with a vector **n** normal to the area **s**. The vector connecting $\boldsymbol{x}_P$ and any other point $\boldsymbol{x}_M$ in **s** is $\boldsymbol{r}_{PM}.\mathbf{v}_P$ and $\mathbf{v}_M$ are the fluid velocities in the corresponding cells. Iso-counters $|\Gamma_2| = 0.5$ are used to identify the boundary of the vortexes. Vortices' core are recognized as the cells of $|\Gamma_1| = 0.8$. According to the computation grid used in this study, eddies larger than $5\times5$grid cells can be detected visually and are shown Fig. 11.

## Appendix 3: Segment resistance

The resistance of each segment against the fluid flow is defined as the ratio of pressure drop across that segment to $L\mu U$. For instance, the resistance of the contraction can be estimated as follows. Combining Eqs. (6) and (7), we have:

$$\frac{\eta^{\mathrm{C}}}{\left(1/\eta^{\mathrm{C}}+1/\eta^{\mathrm{t}}+1/\eta^{\mathrm{E}}\right)^{-1}}=\frac{\Delta P_{ij}}{\Delta P^{\mathrm{C}}}. \tag{28}$$

Multiplying both sides by $K_{\mathrm{app}}^{-1}=\Delta P/L\mu U$, one has:

$$K_{\mathrm{app}}^{-1}\frac{\left(1/\eta^{\mathrm{C}}+1/\eta^{\mathrm{t}}+1/\eta^{\mathrm{E}}\right)^{-1}}{\eta^{\mathrm{C}}}=\frac{\Delta P^{C}}{L\mu U}\frac{\Delta P}{\Delta P_{ij}}. \tag{29}$$

Knowing that $\Delta P^{\mathrm{C}} = \Delta P^{\mathrm{C}} + \Delta\breve{P}^{\mathrm{C}}$ and $\Delta P_{ij} = \Delta P_{ij} + \widetilde{\Delta P_{ij}}$ where $\langle m\rangle$ denotes average of $m$ in the network and over tilde stands for deviation from the average value with the property of $\langle\tilde{m}\rangle = 0$.

Averaging Eq. (27) results in

$$K_{\mathrm{app}}^{-1}\left\langle\frac{\left(1/\eta^{\mathrm{C}}+1/\eta^{\mathrm{t}}+1/\eta^{\mathrm{E}}\right)^{-1}}{\eta^{\mathrm{C}}}\right\rangle = \left\langle\frac{\Delta P^{\mathrm{C}}}{L\mu U}\right\rangle\overbrace{\left\langle\frac{\Delta P}{\Delta P_{ij}}\right\rangle}^{\mathrm{SFA}}+\left\langle\frac{\Delta P}{L\mu U}\right\rangle\left\langle\Delta\breve{P}^{\mathrm{C}}\widetilde{\frac{1}{\Delta P_{ij}}}\right\rangle. \tag{30}$$

Neglecting the second correlation term on the RHS and using the smooth field approximation (SFA) for $\frac{\Delta P}{\Delta P_{ij}}$, we have:

$$K_{\mathrm{app}}^{-1}\left\langle\frac{\left(1/\eta^{\mathrm{C}}+1/\eta^{\mathrm{t}}+1/\eta^{\mathrm{E}}\right)^{-1}}{\eta^{\mathrm{C}}}\right\rangle=\left(\frac{\Delta P^{\mathrm{C}}}{L\mu U}\right)=K_{\mathrm{app}}^{\mathrm{C}^{-1}}, \tag{30}$$

which is the resistance of the contraction section in the network.

**Acknowledgements** The authors would gratefully acknowledge Dr. Behzad Vaferi at Islamic Azad University of Shiraz for his comments on the manuscript and performing some additional analysis in obtaining Eq. (21).

**Funding** Not applicable.

**Availability of data and material** Any material and data can be included.

**Code availability** Matlab: 09806-07443-58955-64350-22751-41297.

## Declarations

**Conflict of interest** Not applicable.

## References

Abdelall FF et al (2005) Pressure drop caused by abrupt flow area changes in small channels. Exp Thermal Fluid Sci 29(4):425–434

Adloo H et al (2015) Development of pore network method in simulation of non-catalytic gas–solid reactions—study of sulfur dioxide chemisorption on copper oxide sorbents. Chem Eng Sci 262:29–312

Adloo H, L'Heureux I, Kharaghani A (2019) Effects of correlated morphological and topological heterogeneity of pore network on effective transport and reaction parameters. Chem Eng Sci 207:280–304. https://doi.org/10.1016/j.ces.2019.05.029

Aramideh, S., P.P. Vlachos, and A.M. Ardekani, Pore-scale statistics of flow and transport through porous media. Physical Review E, 2018. 98(1): p. 013104.

Balhoff MT, Wheeler MF (2009) A predictive pore-scale model for non-Darcy flow in porous media. SPE J 14(04):579–587

Baychev TG et al (2019) Reliability of algorithms interpreting topological and geometric properties of porous media for pore network modelling. Transp Porous Media 128(1):271–301

Blunt MJ et al (2002) Detailed physics, predictive capabilities and macroscopic consequences for pore-network models of multiphase flow. Adv Water Resour 25(8):1069–1089

Bullen PR et al (1987) The determination of pipe contraction pressure loss coefficients for incompressible turbulent flow. Int J Heat Fluid Flow 8(2):111–118

Bultreys T, De Boever W, Cnudde V (2016) Imaging and image-based fluid transport modeling at the pore scale in geological materials: a practical introduction to the current state-of-the-art. Earth Sci Rev 155:93–128

Chalfi TY, Ghiaasiaan SM (2008) Pressure drop caused by flow area changes in capillaries under low flow conditions. Int J Multiph Flow 34(1):2–12

Cheng Z et al (2019) The effect of pore structure on non-Darcy flow in porous media using the lattice Boltzmann method. J Petrol Sci Eng 172:391–400

Chukwudozie C, Tyagi M (2013) Pore scale inertial flow simulations in 3-D smooth and rough sphere packs using lattice Boltzmann method. AIChE J 59(12):4858–4870

Costa TB, Kennedy K, Peszynska M (2018) Hybrid three-scale model for evolving pore-scale geometries. Comput Geosci 22(3):925–950

Dong H, Blunt MJ (2009) Pore-network extraction from micro-computerized-tomography images. Phys Rev E 80(3):036307

Dybbs A, Edwards RV (1984) A new look at porous media fluid mechanics—Darcy to turbulent. In: Bear J, Corapcioglu MY (eds)

Fundamentals of transport phenomena in porous media. Springer, Netherlands, Dordrecht, pp 199–256
El-Zehairy AA et al (2019) Pore-network modelling of non-Darcy flow through heterogeneous porous media. Adv Water Resours 131:103378
Epps B (2017) Review of vortex identification methods. In: 55th AIAA Aerospace Sciences Meeting. American Institute of Aeronautics and Astronautics
Fourar M et al (2004) On the non-linear behavior of a laminar single-phase flow through two and three-dimensional porous media. Adv Water Resour 27(6):669–677
Graftieaux L, Michard M, Grosjean N (2001) Combining PIV, POD and vortex identification algorithms for the study of unsteady turbulent swirling flows. Meas Sci Technol 12(9):1422–1429
Hassanizadeh SM, Gray WG (1987) High velocity flow in porous media. Transp Porous Media 2(6):521–531
Icardi M et al (2014) Pore-scale simulation of fluid flow and solute dispersion in three-dimensional porous media. Phys Rev E 90(1):013032
Joekar-Niasar V et al. (2010) Network model investigation of interfacial area, capillary pressure and saturation relationships in granular porous media. Water Resour Res. 46(6)
Kanda H, Shimomukai K (2009) Numerical study of pressure distribution in entrance pipe flow. J Complex 25(3):253–267
Koponen A, Kataja M, Timonen J (1996) Tortuous flow in porous media. Phys Rev E 54(1):406–410
Lahooti M, Kim D (2019) Multi-body interaction effect on the energy harvesting performance of a flapping hydrofoil. Renewable Energy 130:460–473
Lao H-W, Neeman HJ, Papavassiliou DV (2004) A pore network model for the calculation of non-Darcy flow coefficients in fluid flow through porous media. Chem Eng Commun 191(10):1285–1322
Lasseux D, Valdés-Parada FJ (2017) On the developments of Darcy's law to include inertial and slip effects. Comp Rend Mécan 345(9):660–669
Lemley EC, Papavassiliou DV, Neeman HJ (2007a) Non-Darcy flow pore network simulation: development and validation of a 3D model. (42894), pp. 1331–1337
Lemley EC, Papavassiliou DV, Neeman HJ (2007b) Simulations to determine laminar loss coefficients in arbitrary planar dividing flow geometries. (42894), pp. 1323–1330
Liu R, Li B, Jiang Y (2016) Critical hydraulic gradient for nonlinear flow through rock fracture networks: the roles of aperture, surface roughness, and number of intersections. Adv Water Resour 88:53–65
Lu XKA, Adloo H, Tsotsas E (2020) The Brooks and Corey capillary pressure model revisited from pore network simulations of capillarity-controlled invasion percolation process. Processes 8(10):1308
Ma H, Ruth DW (1993) The microscopic analysis of high Forchheimer number flow in porous media. Transp Porous Media 13(2):139–160
Miao X, Gerke KM, Sizonenko TO (2017) A new way to parameterize hydraulic conductances of pore elements: a step towards creating pore-networks without pore shape simplifications. Adv Water Resour 105:162–172
Muljadi BP et al (2016) The impact of porous media heterogeneity on non-Darcy flow behaviour from pore-scale simulation. Adv Water Resour 95:329–340
Newman MS, Yin X (2013) Lattice Boltzmann simulation of non-Darcy flow in stochastically generated 2D porous media geometries. SPE J 18(01):12–26
Nissan A, Berkowitz B (2018) Inertial effects on flow and transport in heterogeneous porous media. Phys Rev Lett 120(5):054504
Rabbani A, Babaei M (2019) Hybrid pore-network and lattice-Boltzmann permeability modelling accelerated by machine learning. Adv Water Resour 126:116–128
Raeini AQ, Blunt MJ, Bijeljic B (2014) Direct simulations of two-phase flow on micro-CT images of porous media and upscaling of pore-scale forces. Adv Water Resour 74:116–126
Raeini AQ, Bijeljic B, Blunt MJ (2017) Generalized network modeling: network extraction as a coarse-scale discretization of the void space of porous media. Phys Rev E 96(1):013312
Ruth D, Ma H (1992) On the derivation of the Forchheimer equation by means of the averaging theorem. Transp Porous Media 7(3):255–264
Scheibe TD et al (2015) Pore-scale and multiscale numerical simulation of flow and transport in a laboratory-scale column. Water Resour Res 51(2):1023–1035
Skjetne E, Auriault J-L (1999) High-velocity laminar and turbulent flow in porous media. Transp Porous Media 36(2):131–147
Talon L et al (2012) Assessment of the two relaxation time Lattice-Boltzmann scheme to simulate Stokes flow in porous media. Water Resour Res 48(4):W02546s
Thauvin F, Mohanty KK (1998) Network modeling of non-Darcy flow through porous media. Transp Porous Media 31(1):19–37
Valvatne PH, Blunt MJ (2004) Predictive pore-scale modeling of two-phase flow in mixed wet media. Water Resour Res 40(7):W07406
Veyskarami M, Hassani AH, Ghazanfari MH (2016) Modeling of non-Darcy flow through anisotropic porous media: Role of pore space profiles. Chem Eng Sci 151:93–104
Veyskarami M, Hassani AH, Ghazanfari MH (2018) A new insight into onset of inertial flow in porous media using network modeling with converging/diverging pores. Comput Geosci 22(1):329–346
Wang X, Thauvin F, Mohanty KK (1999) Non-Darcy flow through anisotropic porous media. Chem Eng Sci 54(12):1859–1869
White MF (2005) Fluid mechanics, 5th edn. McGraw Hill, New York
Yi Z et al (2017) Pore network extraction from pore space images of various porous media systems. Water Resour Res 53(4):3424–3445